62 64854
CONFIDENTIAL
DECLASSIFIED

Copy 437
RM L58G21

NACA RM L58G21

64 p.

N63 20529
CODE-1

NACA

RESEARCH MEMORANDUM

HEAT TRANSFER MEASURED IN FREE FLIGHT ON A SLIGHTLY BLUNTED 25° CONE-CYLINDER-FLARE CONFIGURATION AT MACH NUMBERS UP TO 9.89

By Dorothy B. Lee, Charles B. Rumsey, and Aleck C. Bond

Langley Aeronautical Laboratory
Langley Field, Va.

OTS PRICE
XEROX $ 6.60 ph
MICROFILM $ 2.12 mf

CLASSIFICATION CHANGED FROM
CONFIDENTIAL TO UNCLASSIFIED--
AUTHORITY NASA-CCN 5-EFFECTIVE
17 JULY 63, JIM CARROLL
DOC. INC.

CLASSIFIED DOCUMENT

This material contains information affecting the National Defense of the United States within the meaning of the espionage laws, Title 18, U.S.C., Secs. 793 and 794, the transmission or revelation of which in any manner to an unauthorized person is prohibited by law.

NATIONAL ADVISORY COMMITTEE FOR AERONAUTICS

WASHINGTON

September 26, 1958

CONFIDENTIAL

DECLASSIFIED

NATIONAL ADVISORY COMMITTEE FOR AERONAUTICS

RESEARCH MEMORANDUM

HEAT TRANSFER MEASURED IN FREE FLIGHT ON A SLIGHTLY BLUNTED 25° CONE-CYLINDER-FLARE CONFIGURATION AT MACH NUMBERS UP TO 9.89*

By Dorothy B. Lee, Charles B. Rumsey, and Aleck C. Bond

SUMMARY

Skin temperatures and surface pressures have been measured at a number of locations on a slightly blunted cone-cylinder-flare configuration at Mach numbers up to 9.89 at corresponding free-stream Reynolds numbers per foot up to 1.21×10^6.

At the higher Mach numbers (above approximately 4.5) the model was not at zero angle of attack. Theoretical values of heating rates are in very good agreement with the experimental data prior to the occurrence of angle of attack. At the higher Mach numbers theoretical predictions of heating rates on the upwind and downwind side of the conical nose agree well with the measured data when effective angles of attack are assumed.

Local transition Reynolds numbers measured on this slightly blunt nose configuration were similar to those previously measured on a sharp nose configuration which was more slender but had similar surface roughness conditions.

INTRODUCTION

Aerodynamic heating on missiles at supersonic and hypersonic speeds is currently being investigated by the Langley Pilotless Aircraft Research Division by means of rocket-propelled models in free flight. A phase of these investigations has dealt with the study of heating and transition on cones and subsequently on cone-cylinder-flare configurations. Reference 1 reports the first test in which heat-transfer data were obtained along the entire cone-cylinder-flare body at Mach numbers up to 4.7.

*Title, Unclassified.

As an extension of this work, a second cone-cylinder-flare configuration similar to that of reference 1 was flight tested at Mach numbers up to 9.89 to obtain heating and transition data at high Mach numbers. The preliminary results of the test were presented in reference 2 which reported the pressure and skin-temperature measurements obtained on the slightly blunted 25° cone, the cylinder, and the 10° half-angle flare. These data were presented in this preliminary form to make the results of the high Mach number test available as soon as possible. The present report presents the heat-transfer data obtained from the temperature measurements presented in reference 2. A considerable portion of the basic information given previously concerning model configuration, instrumentation, and propulsion technique is included here for the convenience of the reader.

The flight test was conducted at the Langley Pilotless Aircraft Research Station at Wallops Island, Va.

SYMBOLS

C_p	pressure coefficient, $\dfrac{p - p_o}{0.7M^2p_o}$
c_p	specific heat of air at constant pressure, Btu/lb-°F
c_w	specific heat of wall material, Btu/lb-°F
g	gravitational constant, 32.2 ft/sec^2
M	Mach number
N_{Pr}	Prandtl number
N_{St}	Stanton number, $\dfrac{c_w\rho_w\tau\dfrac{dT_w}{dt}}{(T_{aw} - T_w)gc_p\rho_l V_l}$
p	pressure, lb/sq in.
q	heating rate, Btu/(sq ft)(sec)
R	Reynolds number
r	radius of nose, in.

T	temperature, $^{\circ}R$ (unless otherwise noted)
t	time, sec
V	velocity, ft/sec
V_c	velocity of sound, ft/sec
x	length from zero station, in.
ϵ	emissivity
ρ	density of air, slugs/cu ft
ρ_w	density of wall material, lb/cu ft
σ	Stefan-Boltzman constant, $0.4806 \times 10^{-12} \frac{\text{Btu}}{\text{ft}^2\text{-sec-}(^{\circ}\text{R})^4}$
τ	thickness of wall, ft
η_r	recovery factor

Subscripts:

aw	adiabatic wall
N	nose
o	free stream
t	stagnation
tr	transition
w	wall condition
l	local

[redacted]

MODEL AND INSTRUMENTATION

Model Configuration

The model was a body of revolution 6.68 feet long with a blunted 25° cone-nose section, a cylindrical midsection, and a 10° half-angle flare section. Figure 1 is a sketch showing pertinent details and dimensions of the model. Figures 2 to 4 show photographs of the model. The conical nose was spun from Inconel sheet approximately 0.032 inch thick. The blunt tip was machined from a solid bar of Inconel and welded to the nose skin. The nose was blunted in order to prevent the tip from melting. The three external channels equally spaced around the cylindrical portion of the body provided cable conduits from the telemeter in the nose to the power plugs and antenna at the base of the flare. The cylinder and flare section were both rolled from 0.032-inch-thick Inconel and welded together. The flare skin was backed by balsa wood to aid in maintaining the conical shape.

Prior to assembly, the nose, cylinder, and flare sections were polished and then heat-treated in order to oxidize the skin surface so that its emissivity would not change radically as the skin heated during the flight. The oxide coating was removed from the forward $2\frac{3}{4}$ inches of the blunted nose in an attempt to have laminar flow fully established before encountering the rougher oxided surface, and this portion of the nose was highly polished as can be seen in the photograph of figure 3. The polished area at the base of the nose cone (fig. 3) was a result of smoothing rivet heads after the nose was oxided.

Measurements made with a Physicists Research Company Profilometer indicated surface roughnesses in microinches (rms) were as follows: prior to oxidizing, 3.5 to 7 on the nose cone, 10 to 20 on the cylinder, and 2 to 3 on the flare; after oxidizing, 10 to 12 on the oxidized nose surface and 2 to 3 on the highly polished forward portion of the nose. Roughness measurements were not made on the cylinder and flare after oxidizing.

Instrumentation

Twenty-four temperatures, five pressures, the thrust acceleration, and the drag deceleration were telemetered from the model during flight. The telemeter was located in the nose section and protected from the high nose-skin temperatures reached during the test by a radiation shield which was rolled from 0.032-inch-thick Inconel and spaced approximately 1/4 inch inside the external nose skin.

One pressure orifice was located near the forward end of the nose section, another on the cylinder just forward of the cylinder-flare junction, and three were located along the flare section, at the stations indicated in figure 1. All the orifices were located on a longitudinal line midway between two of the external channels in order to minimize any influence of the channels on the pressures measured on the flare.

Twenty-three thermocouples were installed on the skin of the model at the locations indicated in figure 1, and one was located on the radiation shield. The eleven thermocouples on the nose skin were located along two longitudinal lines 180° apart circumferentially, six along the upper line, and five at nearly duplicate stations along the lower line. Along the upper line, five thermocouples were also located on the cylinder, and seven on the flare. The upper line was located 120° from the line of the pressure orifices and midway between two channels so as to minimize any influence of orifices and channels on temperature measurements. In order to reduce the heat losses to the balsa backing underneath the flare at the temperature measurement points, cutouts were made in the balsa in the region of each thermocouple. The thermocouples, made of No. 30 chromel-alumel wire, were spot-welded to the inner surface of the skin. During the flight the thermocouple on the radiation shield and several of those on the skin failed to operate or gave quite erratic data and are not reported herein. The measured thicknesses of the Inconel skin at the locations where the thermocouples did operate satisfactorily are given in table I.

During flight, three standard voltages and the outputs of twelve thermocouples were commutated on each of two telemeter channels so that each temperature measurement was recorded about five times per second. The three standard voltages, which were chosen equivalent to the lowest midrange and the highest temperature anticipated, served as an in-flight calibration of the thermocouple telemetering system.

Other instrumentation consisted of ground-based radar units for measuring model velocity and for obtaining the position of the model in space. Velocity data were obtained by means of CW Doppler radar through burnout of the second-stage motor ($t = 29.5$ seconds), and beyond this time model velocity was obtained by integration of telemetered longitudinal acceleration and also by differentiation of the radar flight-path data (up to firing of the fourth-stage motor). These data were obtained from a modified SCR-584 radar which tracked the model until firing of the fourth-stage motor and provided slant range, azimuth, and elevation angle from which altitude, horizontal range, and model flight-path angle were calculated. The range of the SCR-584 radar was extended beyond its normal skin tracking range by use of a modified AN/DPN-19 radar beacon which was installed in the forward end of the third-stage motor. After firing of the fourth-stage motor, the flight-path data were extended by double integration of the telemetered longitudinal-acceleration data.

Atmospheric data and wind conditions were measured to an altitude of 92,800 feet by means of a radiosonde launched near the time of flight and tracked by Rawin set AN/GMD-1A. Standard atmospheric conditions (ref. 3) agreed very well with the measured atmospheric data at the higher altitudes and were used to extend the data through the peak altitude (99,400 feet) of the flight.

PROPULSION AND TEST TECHNIQUE

The propulsion system consisted of four stages of solid-propellant rocket motors. The first and second stages were an M6 JATO rocket motor (Honest John) and M5 JATO rocket motor (Nike), respectively. The third stage was a cluster of three ABL Deacon rocket motors enclosed within a cylindrical skin and the fourth stage was a T-40 Thiokol rocket motor carried within the cylindrical section of the model.

Figure 4 shows the complete assembly on the launcher just prior to firing. The model combination was launched at an elevation angle of 70° and the first two stages were used to boost the third-stage and model to high altitude. Locking devices between the second and third stages and between the third stage and model prevented premature separation of these stages. A peak altitude of 99,400 feet was attained during coasting of the third and fourth stages, and the third stage was fired during the reentry of the model into the denser atmosphere at a flight-path angle of about -4° to the horizontal. About 0.7 second after burnout of the third-stage motor, the fourth stage fired, blasting the model free from the third stage, and accelerated the model to the maximum Mach number of 9.89 at an altitude of 89,600 feet. The firing times for the various stages were chosen to obtain the maximum Mach number without exceeding allowable skin temperatures. A portion of the trajectory that the model followed as well as notations of the various stage firing times is shown in figure 5. The telemeter signal ended 1.5 seconds after maximum Mach number was reached.

Time histories of velocity and altitude for the model through peak velocity are presented in figure 6 and the free-stream velocity of sound, static pressure, temperature, and density are shown in figure 7. The variation of free-stream Mach number and Reynolds number per foot with time is presented in figures 8 and 9, respectively.

DATA REDUCTION

Representative curves of the skin temperatures measured on the nose cone, cylinder, and flare during the flight are shown in figure 10 to

indicate general trends and magnitudes that occurred. The measured temperature data for each station are shown in figures 11 and 12 for the periods when the aerodynamic heating was greatest, that is, between 24 and 42 seconds and between 92 seconds and the end of the test. The measured data indicated by the test points were faired as shown by the solid lines. The local heating rates were then computed by using the measured slopes from the faired curves. The temperature data for the earlier portion of the test are quite regular at each station with a minimum of scatter as can be noted in figure 11. These data are generally within about 5° of the faired curves. However, toward the end of the test, the telemeter signal had begun to get progressively weaker, resulting in considerably more scatter and temporary interruptions in the data of figure 12. The accuracy of these data, both in regard to temperature level and slope, is somewhat less than that of the earlier data.

In order to determine the temperature gradient through the skin, the method of reference 4 was used to compute the outside wall temperature of a typical measurement station during the time period from 94 seconds to the end of the test which was the time period of maximum temperature rise. The results showed a maximum difference of only 14° F between inside and outside wall temperature with the difference generally being less than 5° F. Therefore, the gradients through the skin were neglected in determining the rates of change of skin temperature.

Time histories of experimental aerodynamic heating rates were computed from the faired skin-temperature time histories by the use of the equation

$$q = c_w \rho_w \tau \frac{dT_w}{dt} + \sigma \epsilon T_w^{\,4} \tag{1}$$

where $c_w \rho_w \tau \frac{dT_w}{dt}$ is the time rate of change of heat stored in the model skin, per unit area, and $\sigma \epsilon T_w^{\,4}$ is the external radiation heat-flow term. The specific heat of Inconel c_w and the emissivity ϵ for oxidized Inconel are shown in figure 13 as a function of temperature as obtained from reference 5.

The local theoretical heating rates were computed from the relation

$$q = N_{St}\left(g c_{p,l} \rho_l V_l\right)\left(T_{aw} - T_w\right) \tag{2}$$

Adiabatic wall temperatures were obtained from the relation

$$T_{aw} = \eta_r\left(T_t - T_l\right) + T_l \tag{3}$$

The usual $N_{Pr}^{1/3}$ for turbulent flow and $N_{Pr}^{1/2}$ for laminar flow were used for the theoretical values of η_r with N_{Pr} evaluated at wall temperature. Total temperature T_t was computed from flight conditions with the use of the variation of c_p with temperature.

Values of N_{St} for laminar and turbulent flow were obtained from the theory of Van Driest (ref. 6) as functions of appropriate local Reynolds numbers, Mach numbers, and ratios of $\frac{T_w}{T_l}$, by use of the charts of reference 7. Flat-plate theory was used for the cylinder, and conical theory was used for the nose cone and flare; that is, the length for computation of local Reynolds number was taken as 1/2 cone length plus cylinder length plus 1/2 flare length to the appropriate station for turbulent theory and as 1/3 cone length plus cylinder length plus 1/3 flare length for laminar theory.

Local conditions were determined in the following manner. At the nose-cone stations, static pressure was obtained from sharp-cone theory (ref. 8) and total pressure was taken as that behind a normal shock. Static pressures along the cylinder were obtained from the method of characteristics solutions for cone-cylinder bodies given in reference 9. Total pressure along the cylinder was taken as that behind a conical shock at the nose. This assumption was made because the nose bluntness was small in relation to the length of the nose. Reference 10 shows that for the blunt nose of this test the low Mach number layer is thicker than the laminar boundary layer only on the nose cone. Flow conditions on the flare were determined from the local conditions on the cylinder by the use of conical theory for the shock at the cylinder-flare juncture. The ratios of local static to local total pressure were then used to obtain local Mach number from which local temperature and local density were obtained by the use of perfect gas relations. Tables II, III, and IV give local and free-stream values of M and R per foot and local values of T.

Static pressures measured on the flare are compared in figures 14(a) and 14(b) with theoretical pressures computed for a deflection angle of 10° (flare half-angle) using two-dimensional and three-dimensional theories at the flow conditions at the end of the cylinder. The measured pressures for the early time interval fall between the two- and three-dimensional theoretical pressures as did the pressures measured

on a 10° flare reported in references 1 and 11. During the later time interval the measured pressures oscillate beyond the range of both theories but with the three-dimensional theory approximately averaging the measured pressures. As previously noted, conical flow was assumed to determine the flare local conditions for computation of theoretical heating rates herein. The theoretical heating rates would have been about 20 percent larger if two-dimensional theory had been used. This is due primarily to the difference between two- and three-dimensional static pressure since the difference between two- and three-dimensional total pressure had less than 2 percent influence on the computed theoretical heating rates. It may be noted in figure 14(b) that towards the end of the test the trends of the measured pressures are different from the trends of the theoretical pressures. This is believed to be due to angle of attack which will be discussed later.

RESULTS AND DISCUSSION

Aerodynamic Heating Rates

The comparison of experimental and theoretical aerodynamic heating rates on the nose cone (figs. 15(a) and 15(b)) shows that from 27 seconds to 30 seconds the boundary layer was turbulent as far forward as station 14.18 on the upper line and station 9.54 on the lower line. After 30 seconds, as the Reynolds number on the cone decreased (see table IV), the flow on the entire nose cone became laminar. The experimental laminar and turbulent data for the nose cone are in good agreement with the corresponding theoretical values.

The experimental heating on the cylinder (fig. 15(c)) showed the same trends with time as the rearmost station on the upper side of the nose cone, but with turbulent flow existing longer at the rearward cylinder stations. The turbulent data for the cylinder stations are slightly lower than the turbulent theory. The laminar data are in good agreement with the laminar theory. On the flare (figs. 15(d) and 15(e)), the flow was turbulent as evidenced by the good agreement between experimental and turbulent theoretical heating rates.

Figure 16 shows time histories of the heating rates during the interval from 97 to 106 seconds during which time the pressures of figure 14(b) show oscillations and departures from theoretical predictions for zero angle of attack. Along the upper line on the nose cone (figs. 16(a) and 16(b)), the experimental data at each station became much lower than laminar theory as time progressed. The data along the lower line on the nose cone (figs. 16(c) and 16(d)) became greater than the laminar theory, though not as great as the turbulent theory, as time progressed. This difference from theory is believed to be due to angle

of attack with the upper thermocouple line on the lee side of the body and the lower line on the windward side of the body. This would account for the trends of the nose-cone data during this time period and also for trends observed in data on the flare as will be noted in the following paragraphs.

The heating at the cylinder stations (fig. 16(e)) indicates that the flow remained laminar all along the cylinder.

At each of the flare stations (figs. 16(f) and 16(g)), the data agreed with the turbulent theory at the beginning of the time period. Later during the time interval the experimental heating at the first two stations approached the laminar theory and at the further rearward stations was somewhat below turbulent theory. These trends could be accounted for by an angle of attack with the upper thermocouple line (that is, flare thermocouples) being on the leeward side of the body, as will be noted in connection with the plots showing the distribution of heating along the body at the later times.

Figures 17(a) and 17(b) show the distribution of heating along the body for several times during the earlier time period, 27 to 33 seconds. On the cylinder, the turbulent theoretical rates tend to be slightly higher than the measurements; whereas, on the nose cone and flare, the theoretical heating rates agree very well with the measurements. Reference 12 suggests using local Reynolds number based on length from the cylinder-flare juncture to predict theoretical values for flare heating. These theoretical predictions were higher than the experimental data of reference 12 for a 10° flare but showed good agreement with the experimental data for a 30° flare. Theoretical predictions using Reynolds number based on length from the cylinder-flare juncture for the present test were considerably higher than the flare experimental data as shown in figure 17(a) at $t = 29$ seconds.

Why transition occurred farther forward on the lower line of the nose than on the upper line at times up to 30 seconds is unknown. From 31 seconds on, while the Reynolds number was rapidly decreasing, laminar flow spread over the entire nose and part way back along the cylinder. Transition Reynolds numbers obtained from these plots will be considered later.

Figures 17(c) to 17(f) show the distribution of heating rates along the body at several times during the later period of strong aerodynamic heating. The distributions of heating along the upper and lower surfaces of the cone are generally lower and higher, respectively, than the laminar theory which is for zero angle of attack. On the cylinder, the data are generally in fair agreement with laminar theory. On the flare, the data are in fair agreement with the turbulent theory at 97 and 98 seconds but at later times fall progressively lower than turbulent theory. These

heating trends on the nose and flare suggest that the model was flying at an angle of attack with the upper thermocouple line on the lee side of the body. Theoretical heating rates at the nose-cone thermocouple locations were estimated for angle-of-attack conditions. The assumption was made that the upper and lower thermocouple lines were in the plane of angle of attack and the local conditions along the upper and lower thermocouple lines were assumed to be those on cones with cone half-angle larger and smaller, respectively, than the actual nose cone by the amount of the angle of attack. These local conditions were then used with the measured skin temperatures to compute theoretical heating rates for angles of attack at two times (102 and 104 seconds) which are shown in figure 18. Figure 18(a) shows that at 102 seconds, the theoretical laminar heating rates for an assumed angle of attack of 8.5° agree well with the data measured along both the upper and lower thermocouple lines. Figure 18(b) shows similar agreement at 104 seconds between the measured data and the theoretical computations for an assumed angle of attack of 12.5°. It should be noted that similar agreement between the measurements and computations would exist for a condition of larger angles of attack but with the thermocouple lines displaced in roll from the plane of angle of attack. In fact, the pressures measured on the nose (fig. 19) tend to indicate this condition. The pressures measured 60° circumferentially from the lower (or windward) thermocouple line and 0.63 diameter behind the blunt-nose tip suggest an angle of attack which increased with time, but the values are not as much above the zero-angle-of-attack level as would be expected for a location 60° circumferentially from the upwind element of the cone. Probably the angle of attack was larger than the values assumed in figure 18, but with the thermocouple lines approximately 30° from the plane of the angle of attack (and effectively at the assumed angles) and with the pressure orifice approximately 90° from the plane of the angle of attack. More refined analysis has not been attempted since there are insufficient data or theory in regard to pressure behind a blunt-nose tip.

Estimation of angle-of-attack influence on the flare heating was not made since local conditions on the flare at an angle of attack could not be determined. However, turbulent rates on the leeward side of the flare would be expected to be lower than turbulent rates for zero angle of attack. The experimental data on the flare are lower than zero angle-of-attack turbulent theory prior to 104 seconds but appear to be of turbulent character. After 104 seconds the tendency for the flare heating rates close behind the cylinder-flare juncture to be low may be indicative of separated flow. The pressures measured on the flare 120° circumferentially from the line of thermocouples also indicate the possibility of flow separation in the vicinity of the cylinder-flare juncture after 104 seconds. (See fig. 14(b).)

Transition

Transition data for several flight models are shown in figure 20(a) along with the present data. The models of references 13 and 14 have sharp polished noses and that of reference 1 has a pointed oxidized nose cone with the tip rounded off with a radius of about 0.01 inch. The present test is a slightly blunted oxidized nose cone. At local Mach numbers of 2 and below, the present measurements are lower than transition data for sharp-cone models and appear to be a continuation of the data of reference 1 which had a similar surface roughness though much slimmer bluntness. It appears that blunting did not influence the local transition Reynolds number. When transition moved back on the cylinder, the transition Reynolds number near $M = 3.5$ increased over the nose R_{tr} in a similar fashion to the data of reference 1.

In figure 20(b) the temperature ratio of the present test is lower at $M = 2.0$ than the referenced data and similar at other Mach numbers. It appears that temperature did not have a large influence on the transition Reynolds number.

Transition Reynolds numbers are not shown for the high-speed later portion of the test because of the presence of angle of attack. However, it may be noted from the heating distribution in figures 17(c) to 17(e) that the flow was laminar at least as far back as the last station on the cylinder. The local Reynolds numbers at the last cylinder station based on length from the nose tip with zero-angle-of-attack assumptions varied from 2.5×10^6 to 3.5×10^6 during this later time when the local Mach number varied between 4.6 and 9.0.

CONCLUSIONS

Skin temperatures and surface pressures have been measured at a number of locations on a slightly blunted cone-cylinder-flare configuration at Mach numbers up to 9.89 at corresponding free-stream Reynolds numbers up to 1.21×10^6 per foot. At the higher Mach numbers (above approximately 4.5) the model was not at zero angle of attack. Analysis of the data indicate the following:

1. Theoretical values of heating rates based on conical flow on the nose and flare and flat plate theory for the cylinder are in very good agreement with the experimental data prior to the occurrence of angle of attack.

2. At the higher Mach numbers (above approximately 4.5) theoretical predictions of heating rates on the windward and leeward side of the

conical nose agree well with the measured data when effective angles of attack were assumed.

3. Laminar heating rates were measured at forward locations on the nose cone throughout the test and as far rearward as the last measurement station on the cylinder during low Reynolds number portions of the test.

4. Transitional Reynolds numbers, which varied between 2.8×10^6 and 14.9×10^6, were not greater for this blunted nose configuration than those on a similar sharp-nosed model which had similar surface roughness.

Langley Aeronautical Laboratory,
National Advisory Committee for Aeronautics,
Langley Field, Va., July 9, 1958.

REFERENCES

1. Rumsey, Charles B., and Lee, Dorothy B.: Measurements of Aerodynamic Heat Transfer on a 15° Cone-Cylinder-Flare Configuration in Free Flight at Mach Numbers up to 4.7. NACA RM L57J10, 1958.

2. Bond, Aleck C., and Rumsey, Charles B.: Free-Flight Skin Temperature and Pressure Measurements on a Slightly Blunted 25° Cone-Cylinder-Flare Configuration to a Mach Number of 9.89. NACA RM L57B18, 1957.

3. The Rocket Panel: Pressures, Densities, and Temperatures in the Upper Atmosphere. Phys. Rev., vol. 88, no. 5, Second ser., Dec. 1, 1952, pp. 1027-1032.

4. Hill, P. R.: A Method of Computing the Transient Temperature of Thick Walls From Arbitrary Variation of Adiabatic-Wall Temperature and Heat-Transfer Coefficient. NACA TN 4105, 1957.

5. Ginnings, Defoe C., and Thomas, Eugenia: The Electrical Resistance and Total Radiant Emittance of Inconel in the Range 0° to 1000° C. NBS Rep. 4111 (NACA Contract S54-52), Nat. Bur. Standards, May 1955.

6. Van Driest, E. R.: The Problem of Aerodynamic Heating. Aero. Eng. Rev., vol. 15, no. 10, Oct. 1956, pp. 26-41.

7. Lee, Dorothy B., and Faget, Maxime A.: Charts Adapted From Van Driest's Turbulent Flat-Plate Theory for Determining Values of Turbulent Aerodynamic Friction and Heat-Transfer Coefficients. NACA TN 3811, 1956.

8. Ames Research Staff: Equations, Tables, and Charts for Compressible Flow. NACA Rep. 1135, 1953. (Supersedes NACA TN 1428.)

9. Clippinger, R. F., Giese, J. H., and Carter, W. C.: Tables of Supersonic Flows About Cone Cylinders. Part I: Surface Data. Rep. No. 729, Ballistic Res. Lab., Aberdeen Proving Ground, 1950.

10. Moeckel, W. E.: Some Effects of Bluntness on Boundary-Layer Transition and Heat Transfer at Supersonic Speeds. NACA Rep. 1312, 1957. (Supersedes NACA TN 3653.)

11. Bland, William M., Jr., and Kolenkiewicz, Ronald: Free-Flight Pressure Measurements Over a Flare-Stabilized Rocket Model With a Modified Von Kármán Nose for Mach Numbers up to 4.3. NACA RM L57J24, 1958.

12. Becker, John V., and Korycinski, Peter F.: Heat Transfer and Pressure Distribution at a Mach Number of 6.8 on Bodies With Conical Flares and Extensive Flow Separation. NACA RM L56F22, 1956.

13. Rumsey, Charles B., and Lee, Dorothy B.: Measurements of Aerodynamic Heat Transfer and Boundary-Layer Transition on a 15° Cone in Free Flight at Supersonic Mach Numbers up to 5.2. NACA RM L56F26, 1956.

14. Rumsey, Charles B., and Lee, Dorothy B.: Measurements of Aerodynamic Heat Transfer and Boundary-Layer Transition on a 10° Cone in Free Flight at Supersonic Mach Numbers up to 5.9. NACA RM L56B07, 1956.

TABLE I.- SKIN THICKNESS AT THERMOCOUPLE STATIONS

Station	Thickness, in.
Cone - upper line	
5.64	0.0349
7.59	.0323
9.67	.0307
14.18	.0315
Cone - lower line	
7.53	0.0318
9.54	.0322
11.50	.0329
13.94	.0321
Cylinder	
23.37	0.0321
34.37	.0315
45.37	.0323
58.57	.0337
Flare	
61.09	0.0327
62.77	.0328
64.44	.0329
66.41	.0330
69.37	.0329
73.70	.0324
78.72	.0317

TABLE II.- MACH NUMBER

M_o	t, sec	Local Mach number M_l for -					
		Cone	Cylinder				Flare
		All stations	Station 23.37	Station 34.37	Station 45.37	Station 58.57	All stations
2.09	27	1.60	2.24	2.17	2.14	2.11	1.93
2.97	28	1.89	3.13	3.03	3.01	2.99	2.69
3.50	29	2.01	3.68	3.57	3.55	3.52	3.14
3.44	30	2.00	3.63	3.51	3.49	3.48	3.12
3.39	31	1.99	3.56	3.47	3.44	3.40	3.04
3.33	32	1.98	3.50	3.41	3.38	3.37	3.02
3.27	33	1.96	3.43	3.33	3.30	3.29	2.94
4.59	97	2.17	4.78	4.66	4.62	4.60	4.00
4.84	98	2.20	5.02	4.90	4.87	4.85	4.17
5.58	99	2.27	5.71	5.62	5.58	5.55	4.65
6.29	100	2.32	6.35	6.29	6.24	6.18	5.05
7.04	101	2.35	7.02	6.96	6.89	6.84	5.46
7.88	102	2.37	7.72	7.62	7.58	7.52	5.85
8.83	103	2.40	8.48	8.35	8.33	8.28	6.33
9.61	104	2.43	9.04	8.92	8.89	8.83	6.58
9.88	105	2.43	9.22	9.11	9.06	9.00	6.62
9.86	106	2.43	9.20	9.09	9.05	8.99	6.62

TABLE III.- LOCAL TEMPERATURE

t, sec	Local temperature T_l, °R, on -					
	Cone	Cylinder				Flare
	All stations	Station 23.37	Station 34.37	Station 45.37	Station 58.57	All stations
27	533	403	418	424	427	462
28	680	393	407	414	418	478
29	784	382	395	402	406	479
30	749	372	384	391	395	458
31	717	363	375	382	386	451
32	692	356	368	375	379	436
33	670	353	365	371	375	435
97	1,113	390	402	409	413	516
98	1,199	392	403	411	415	528
99	1,478	399	409	416	421	563
100	1,782	408	417	425	429	607
101	2,154	419	429	436	441	651
102	2,619	433	444	450	453	712
103	3,201	452	462	469	473	766
104	3,725	469	479	486	491	839
105	3,912	475	486	491	498	874
106	3,898	475	485	491	498	871

TABLE IV.- REYNOLDS NUMBER

R_o, per foot	t, sec	Local Reynolds number R_l per foot on -					
		Cone	Cylinder				Flare
		All stations	Station 23.37	Station 34.37	Station 45.37	Station 58.57	All stations
5.82×10^6	27	4.81×10^6	5.41×10^6	5.68×10^6	5.75×10^6	5.79×10^6	6.41×10^6
7.97	28	4.84	7.09	7.45	7.63	7.74	9.45
8.62	29	4.43	7.56	7.90	8.18	8.29	10.74
7.85	30	4.10	6.95	7.23	7.45	7.60	10.08
7.15	31	3.83	6.31	6.65	6.79	6.88	8.83
6.48	32	3.51	5.73	6.02	6.18	6.31	8.23
5.83	33	3.20	5.15	5.40	5.54	5.65	7.17
.53	97	.20	.45	.47	.48	.49	.74
.56	98	.20	.47	.49	.50	.52	.79
.65	99	.19	.52	.54	.56	.57	.92
.73	100	.19	.56	.59	.60	.61	1.04
.84	101	.18	.61	.64	.65	.66	1.22
.94	102	.18	.65	.66	.68	.70	1.33
1.05	103	.18	.67	.69	.71	.72	1.50
1.15	104	.18	.68	.70	.72	.73	1.53
1.21	105	.18	.70	.72	.74	.76	1.55
1.21	106	.18	.70	.72	.74	.76	1.55

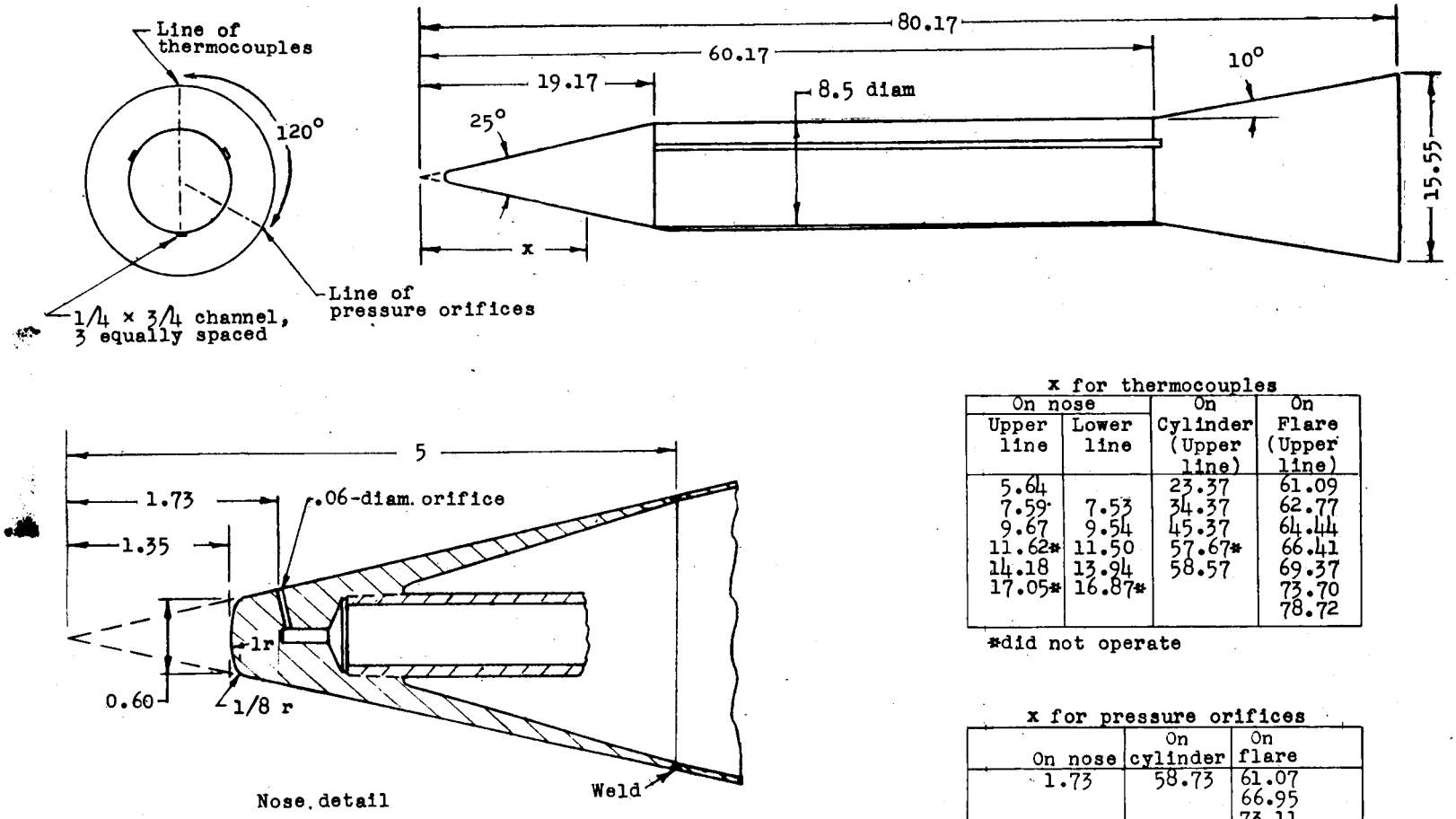

x for thermocouples

On nose		On Cylinder (Upper line)	On Flare (Upper line)
Upper line	Lower line		
5.64		23.37	61.09
7.59	7.53	34.37	62.77
9.67	9.54	45.37	64.44
11.62*	11.50	57.67*	66.41
14.18	13.94	58.57	69.37
17.05*	16.87*		73.70
			78.72

*did not operate

x for pressure orifices

On nose	On cylinder	On flare
1.73	58.73	61.07
		66.95
		73.11

Figure 1.- Sketch of model and detail of nose construction. All dimensions are in inches.

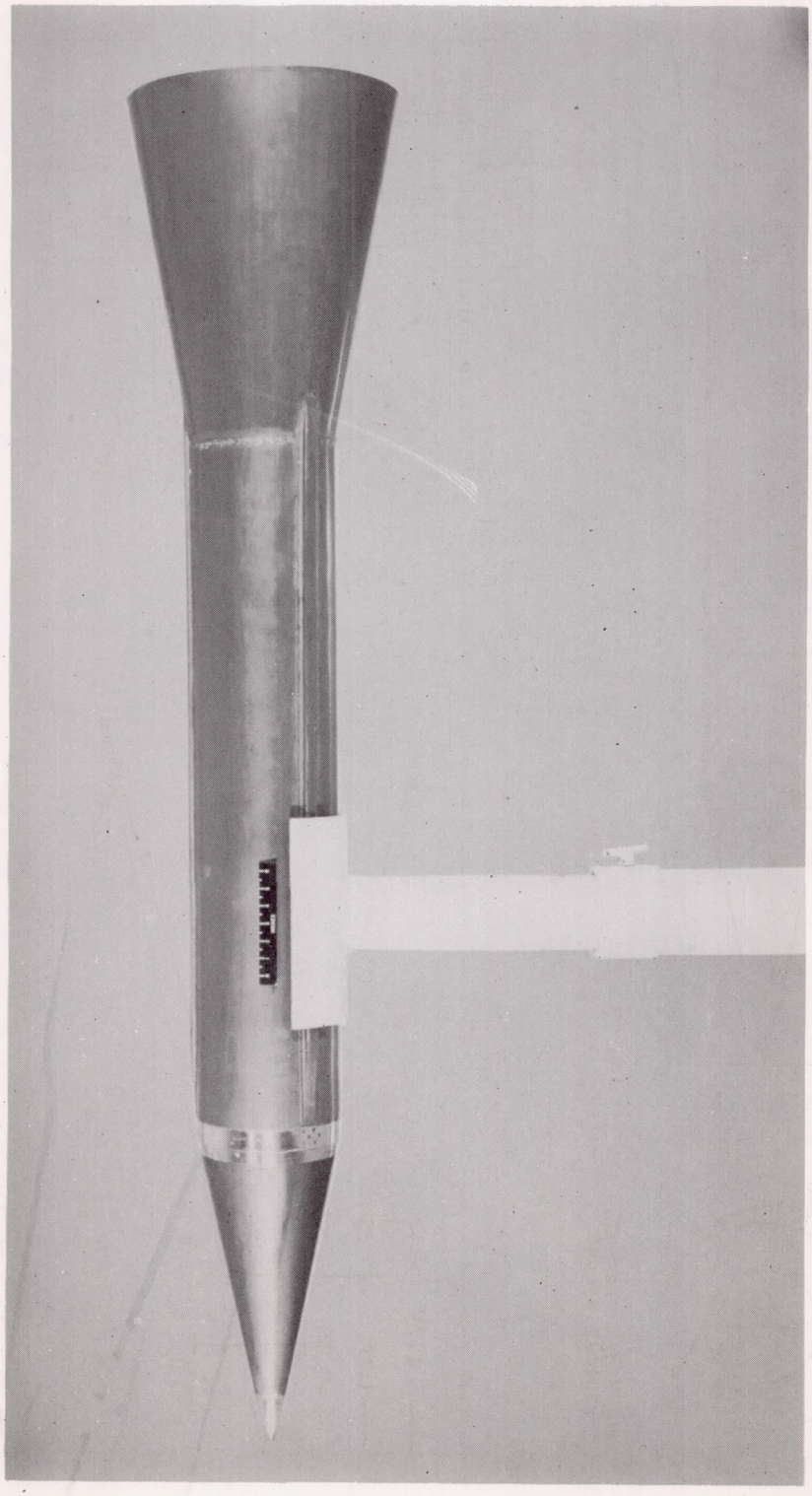

Figure 2.- Photograph of model. L-94556.1

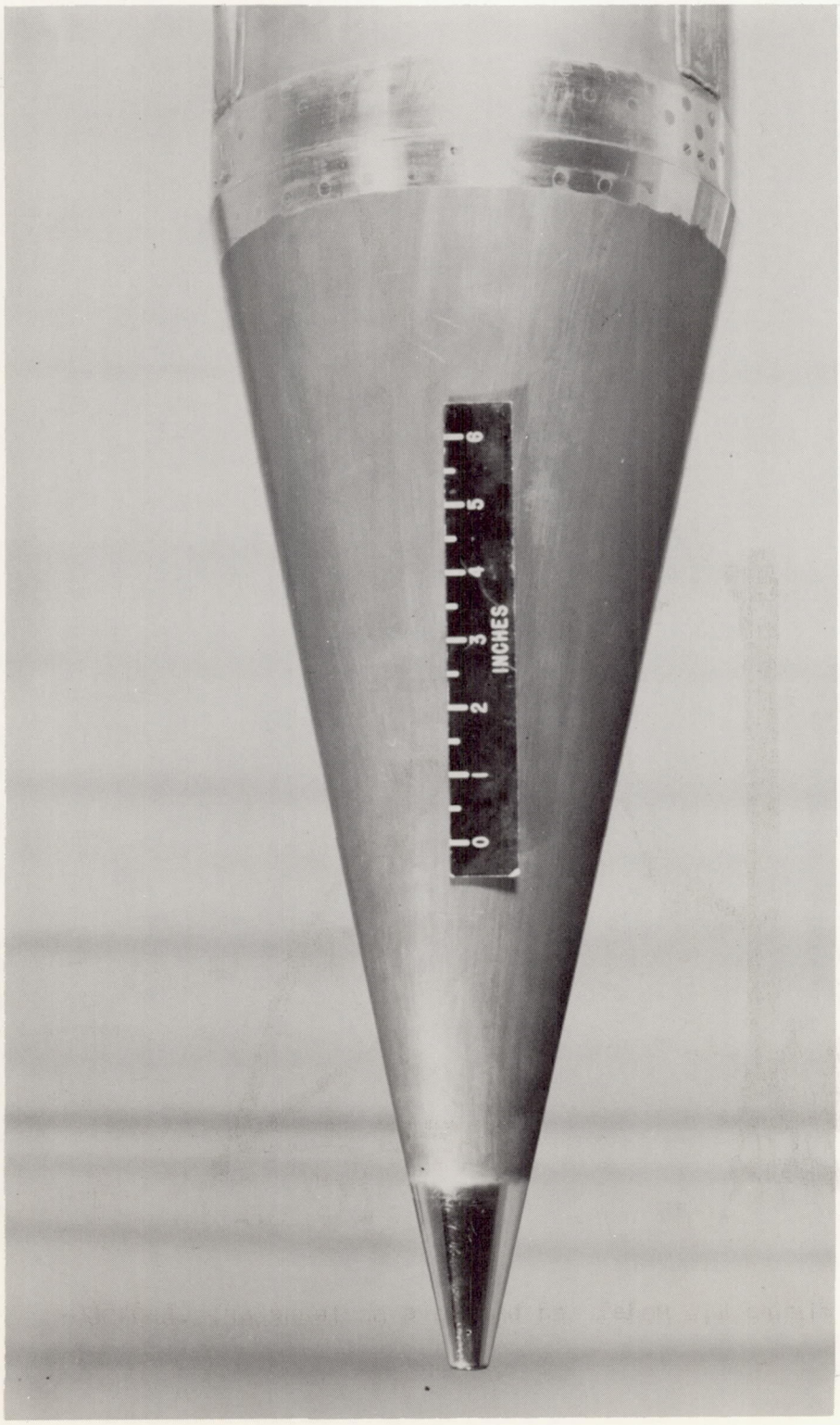

Figure 3.- Closeup photograph of model nose. L-94555

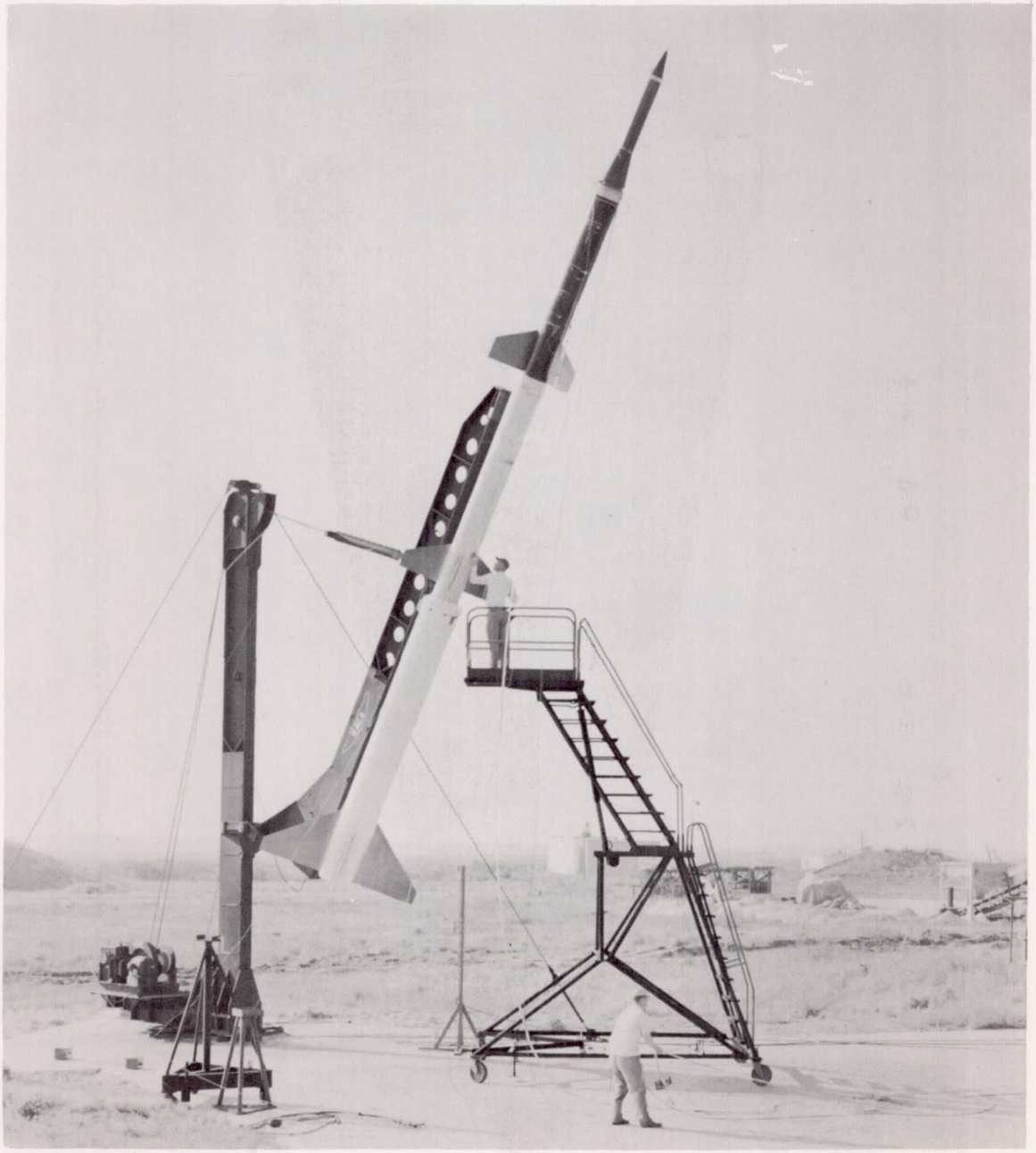

Figure 4.- Model and boosters on launcher. L-94566

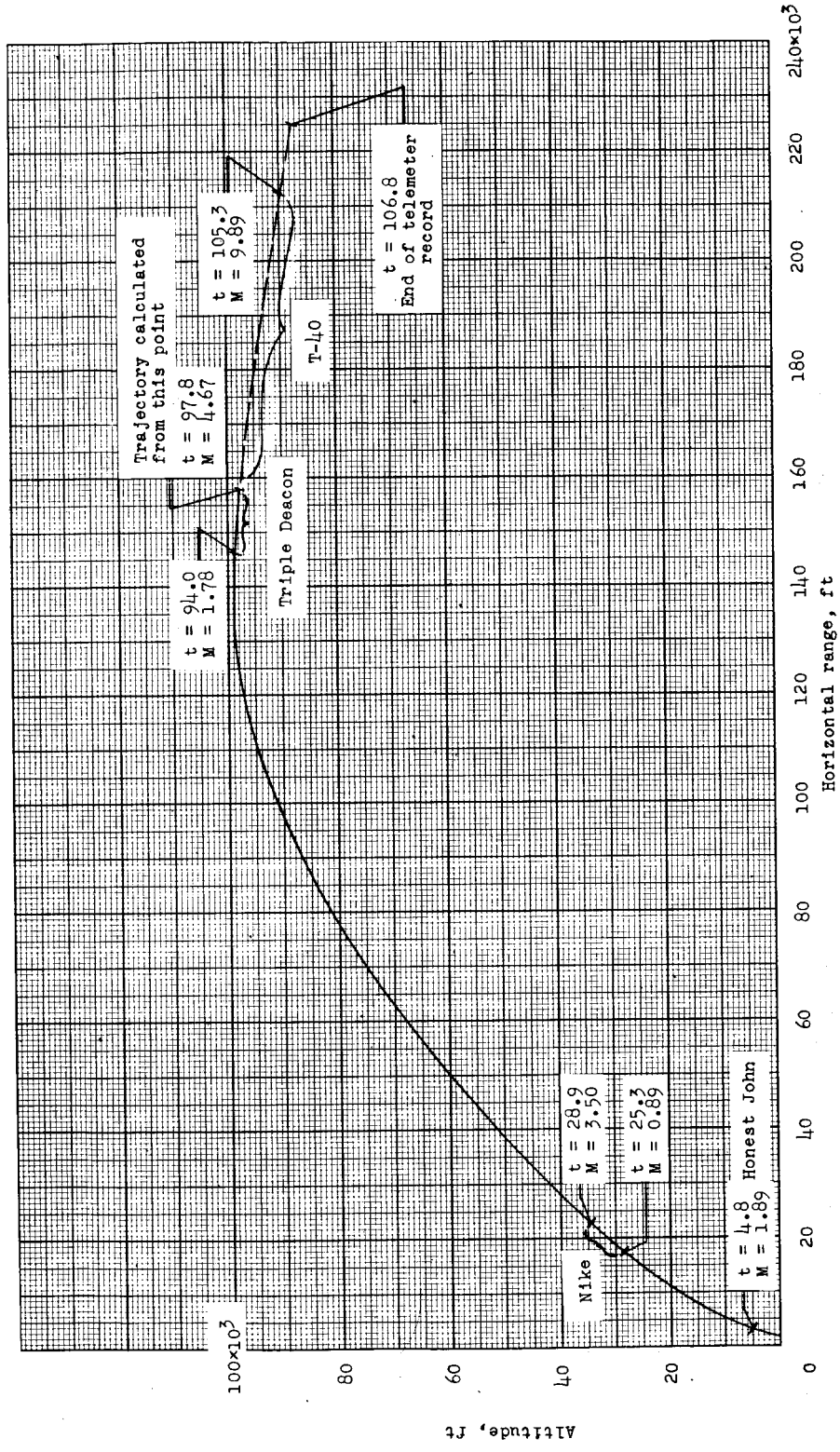

Figure 5.- A portion of the model trajectory.

[redacted]

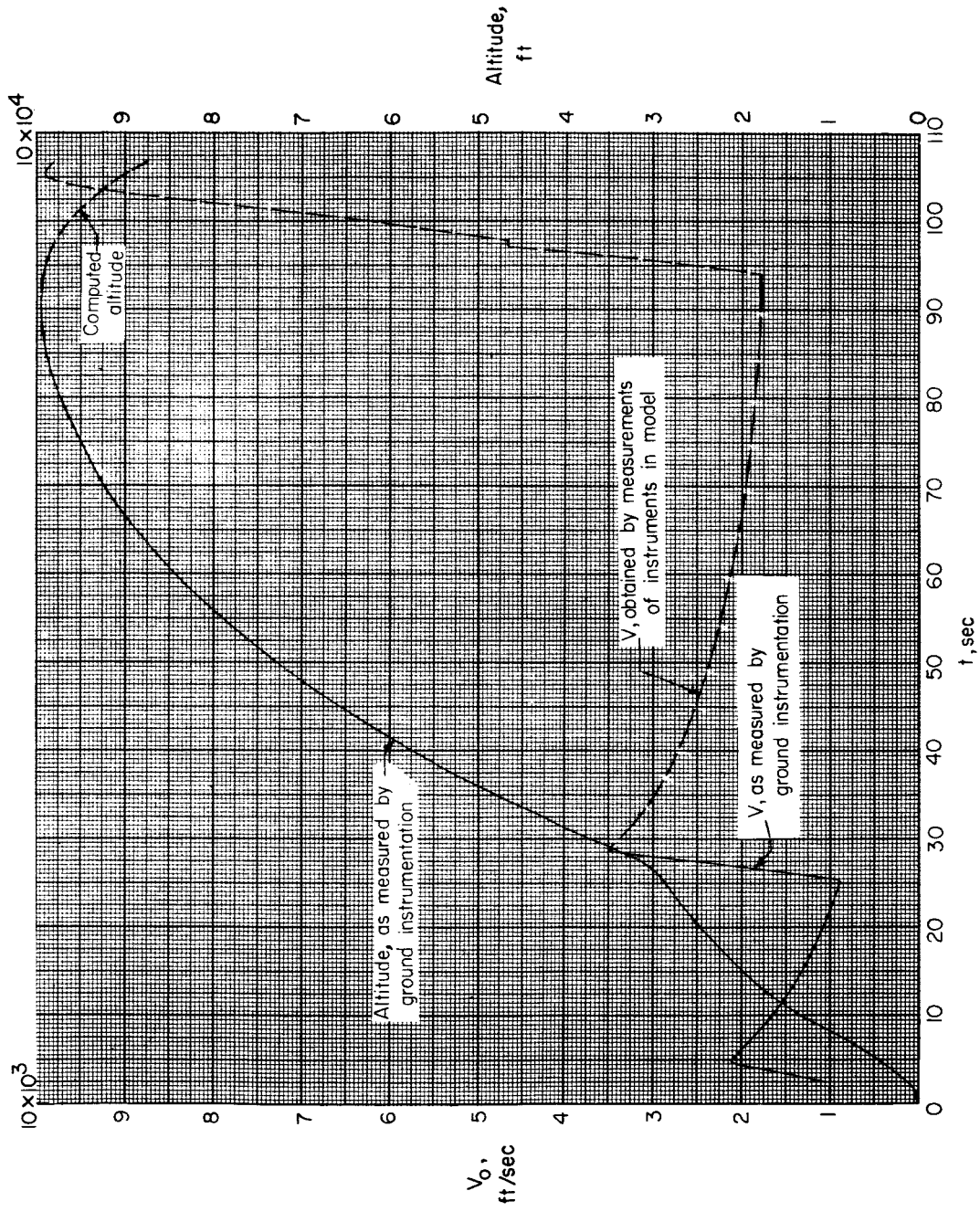

Figure 6.- Variation of altitude and velocity with time for the test vehicle.

[redacted]

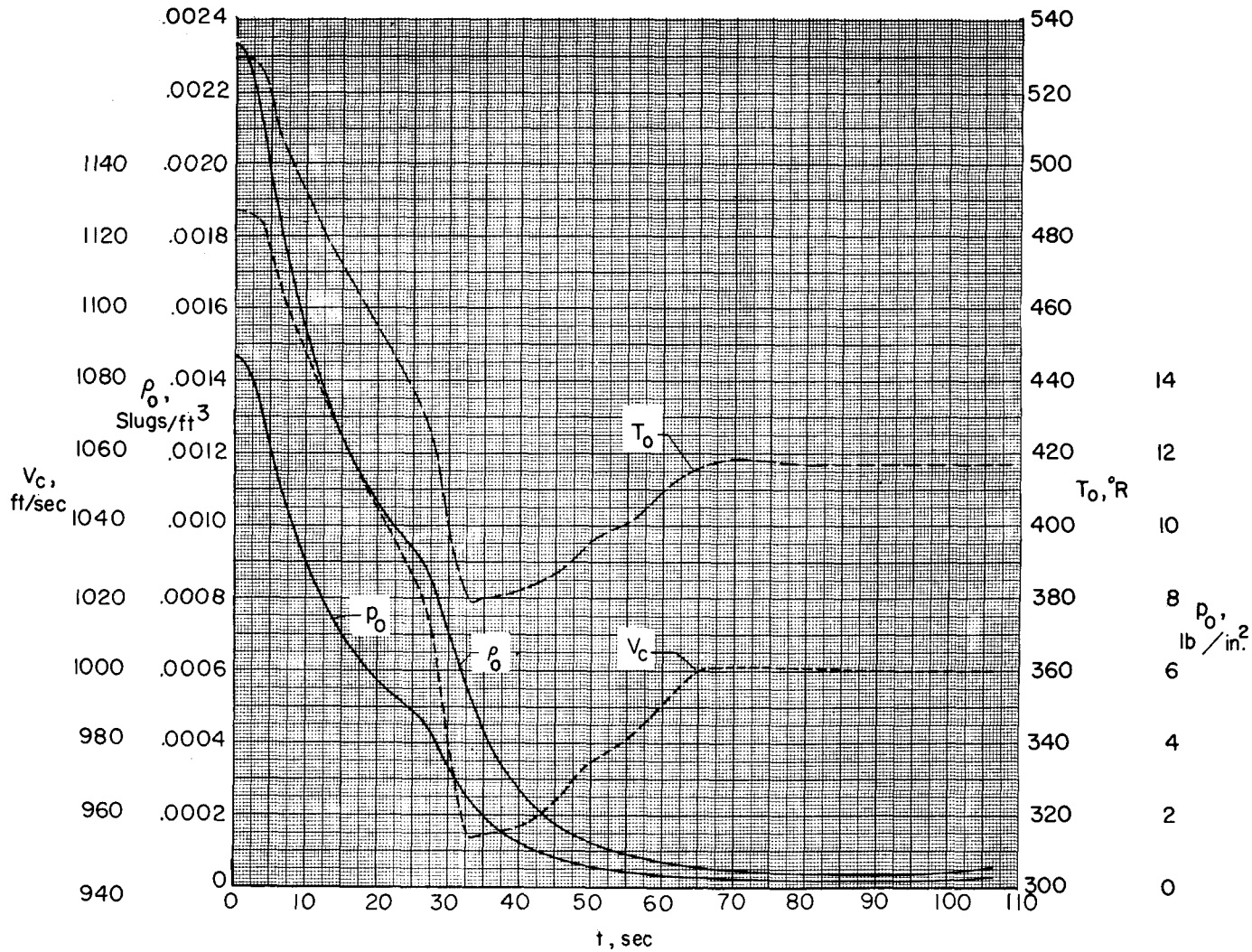

Figure 7.- Time histories of the velocity of sound, density of air, temperature, and static air pressure.

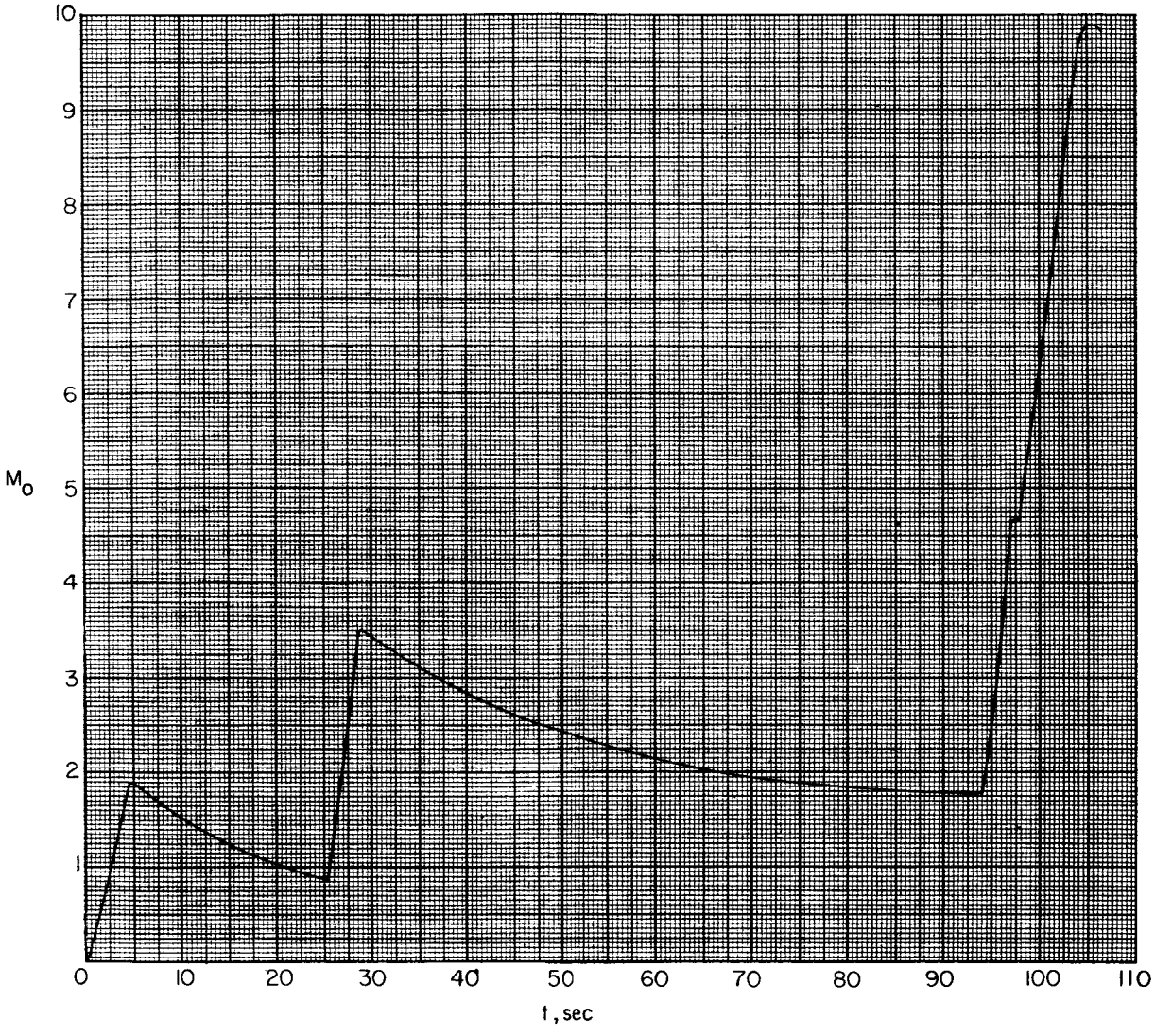

Figure 8.- Variation of Mach number with time for the test vehicle.

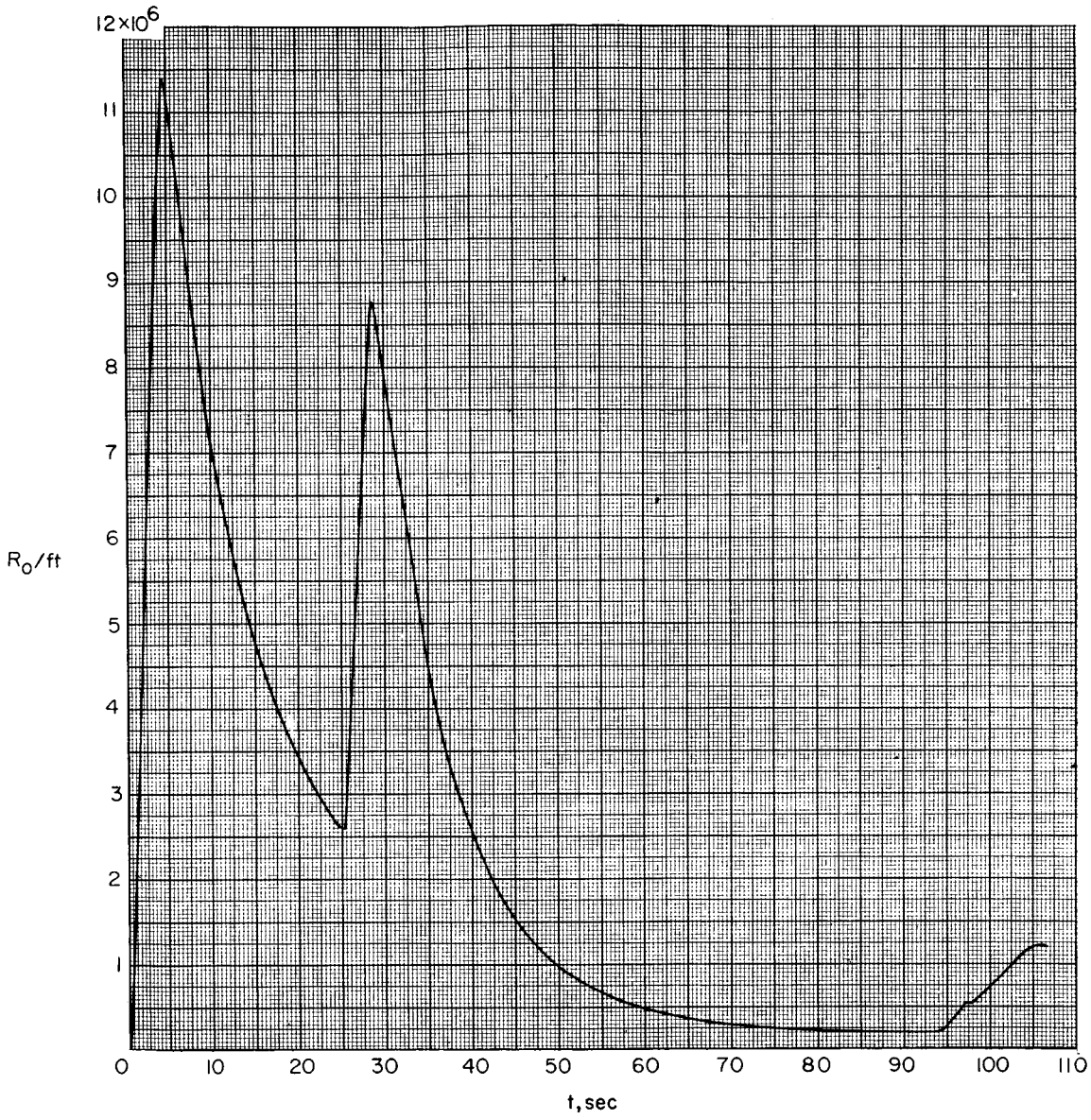

Figure 9.- Variation of Reynolds number per foot with time for the test vehicle.

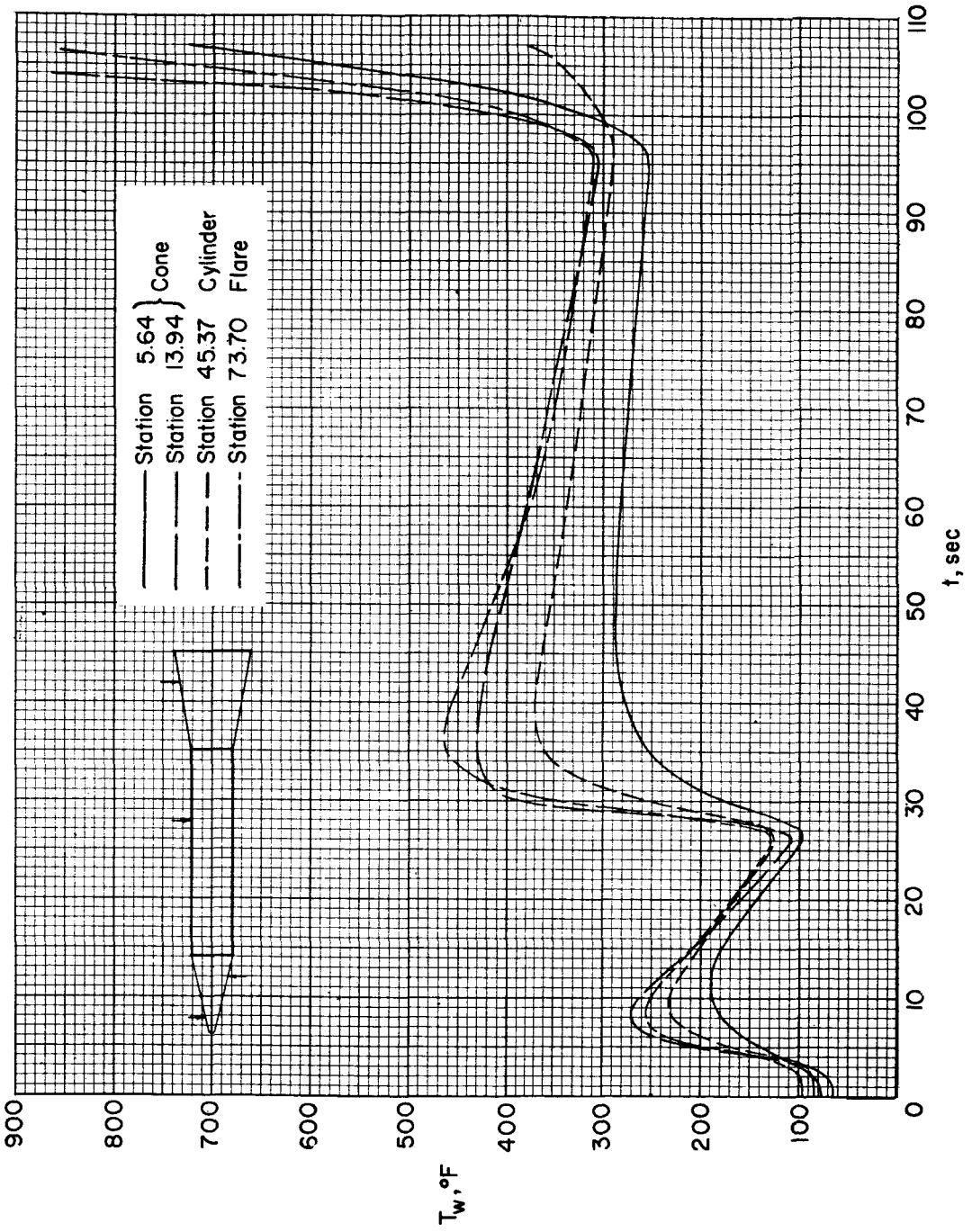

Figure 10.- Typical skin-temperature time histories as obtained from faired measurements.

[redacted]

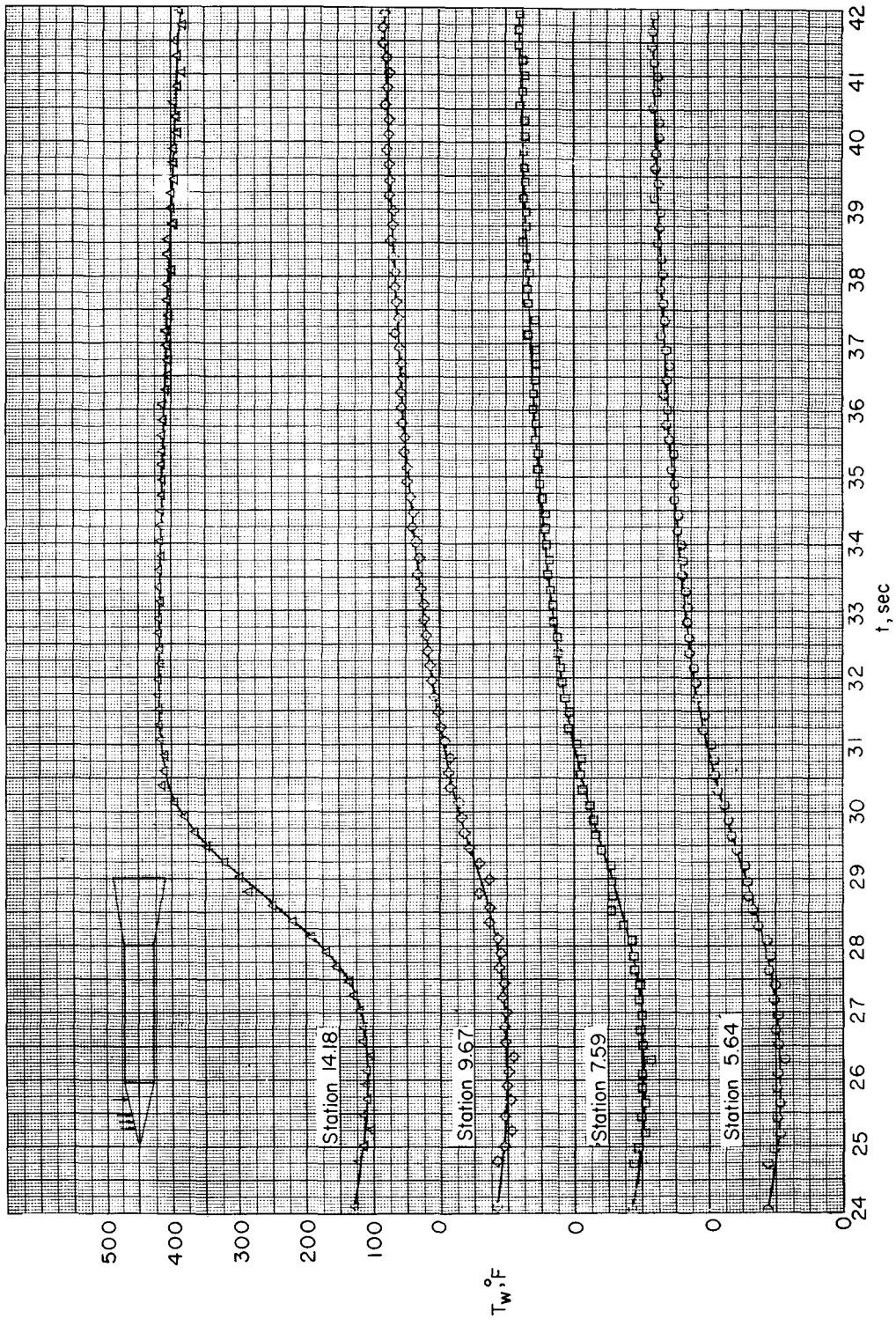

(a) Nose cone stations along upper thermocouple line.

Figure 11.- Time histories of skin temperatures over the period including the second-stage firing.

[redacted]

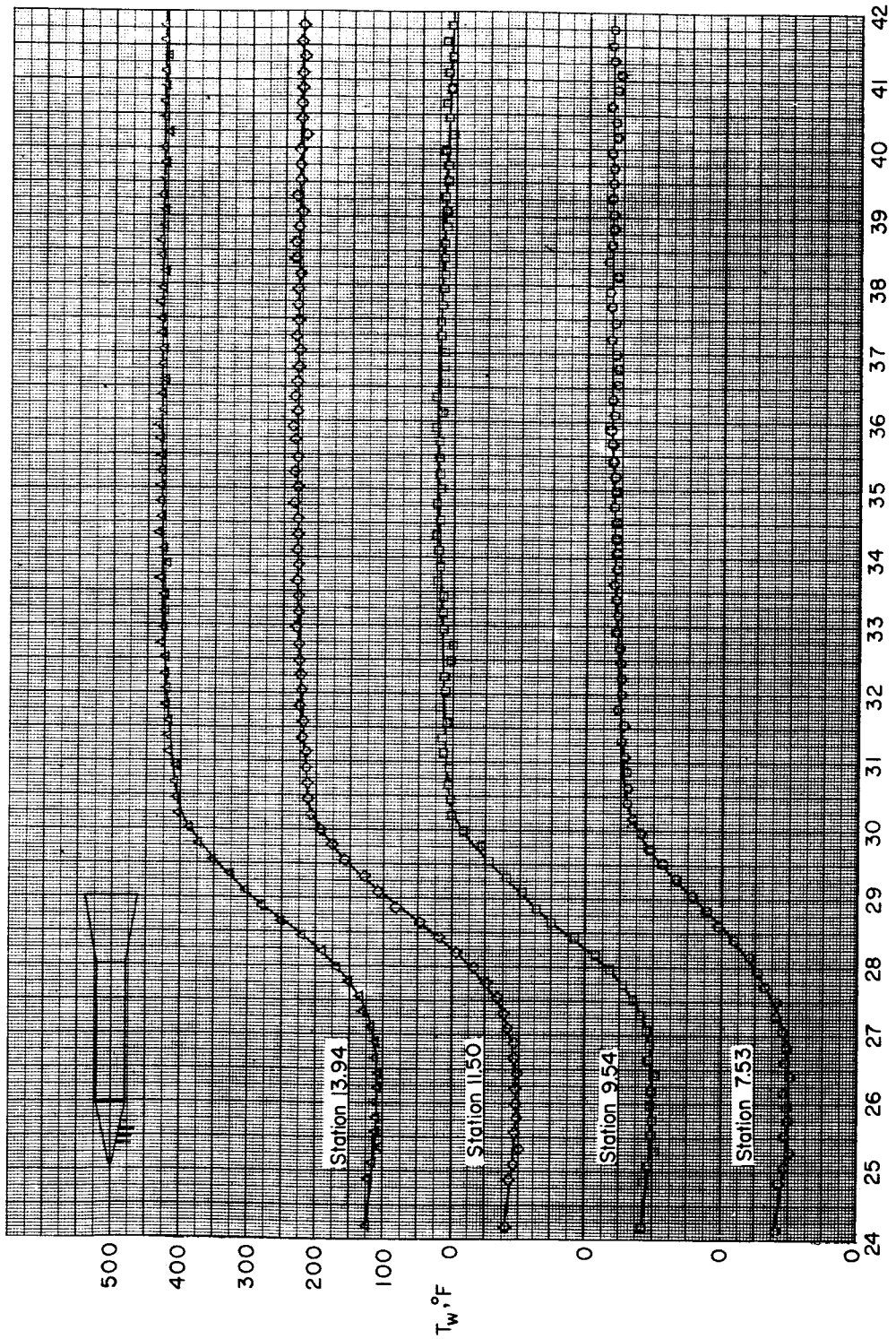

(b) Nose cone stations along lower thermocouple line.

Figure 11.- Continued.

[redacted]

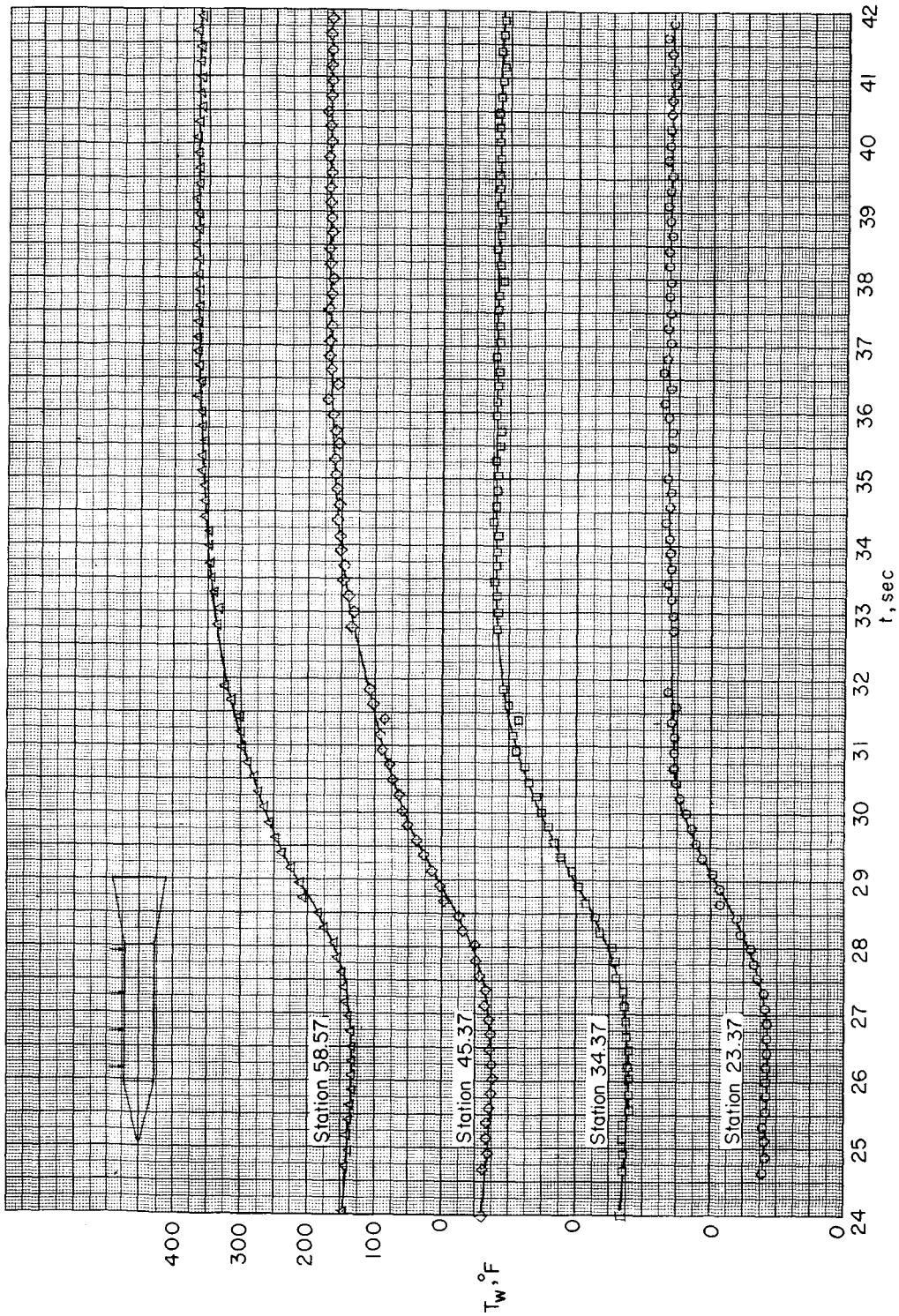

(c) Cylinder stations.

Figure 11.- Continued.

[redacted]

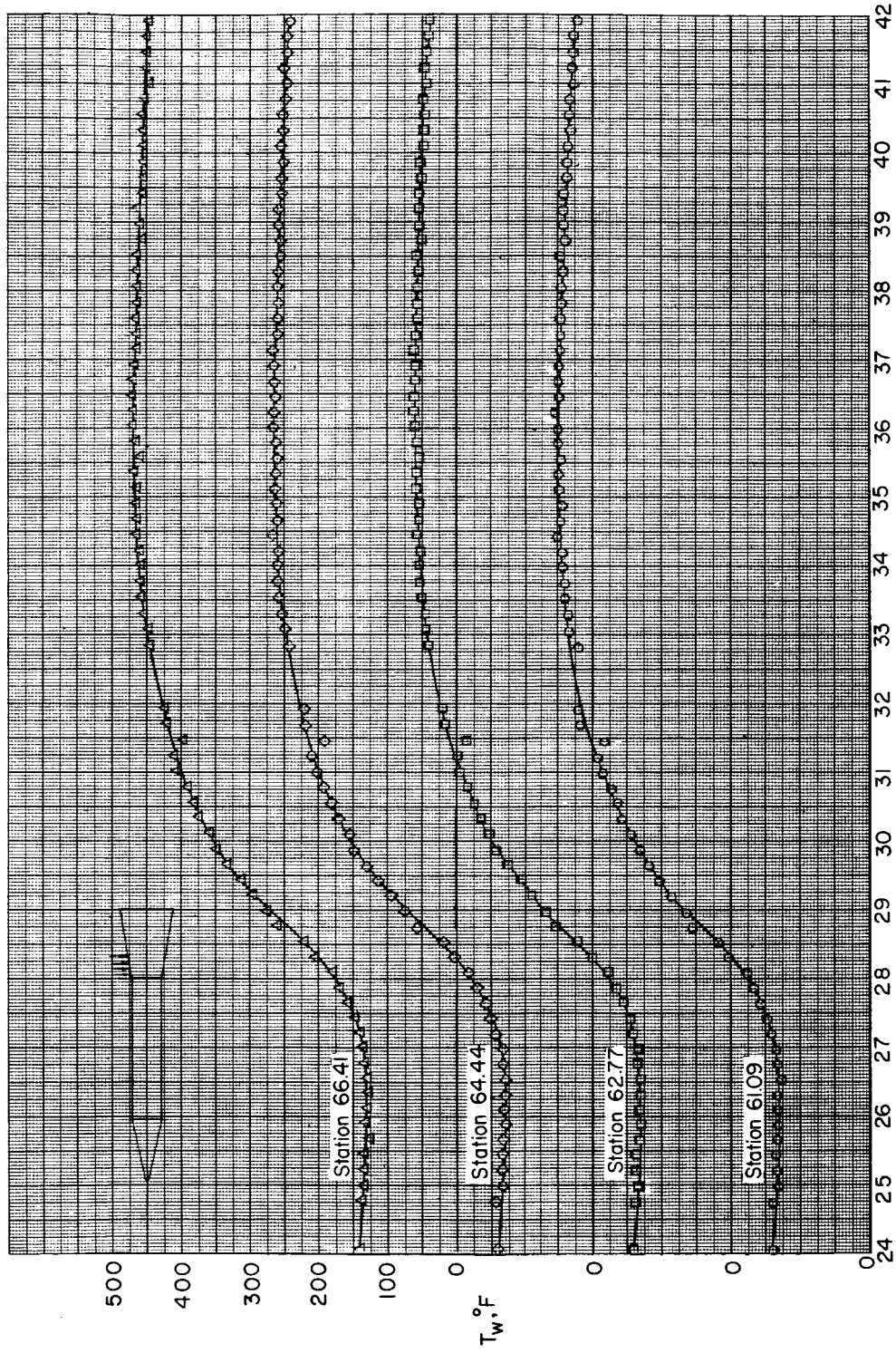

(d) Stations on forward part of flare.

Figure 11.- Continued.

[redacted]

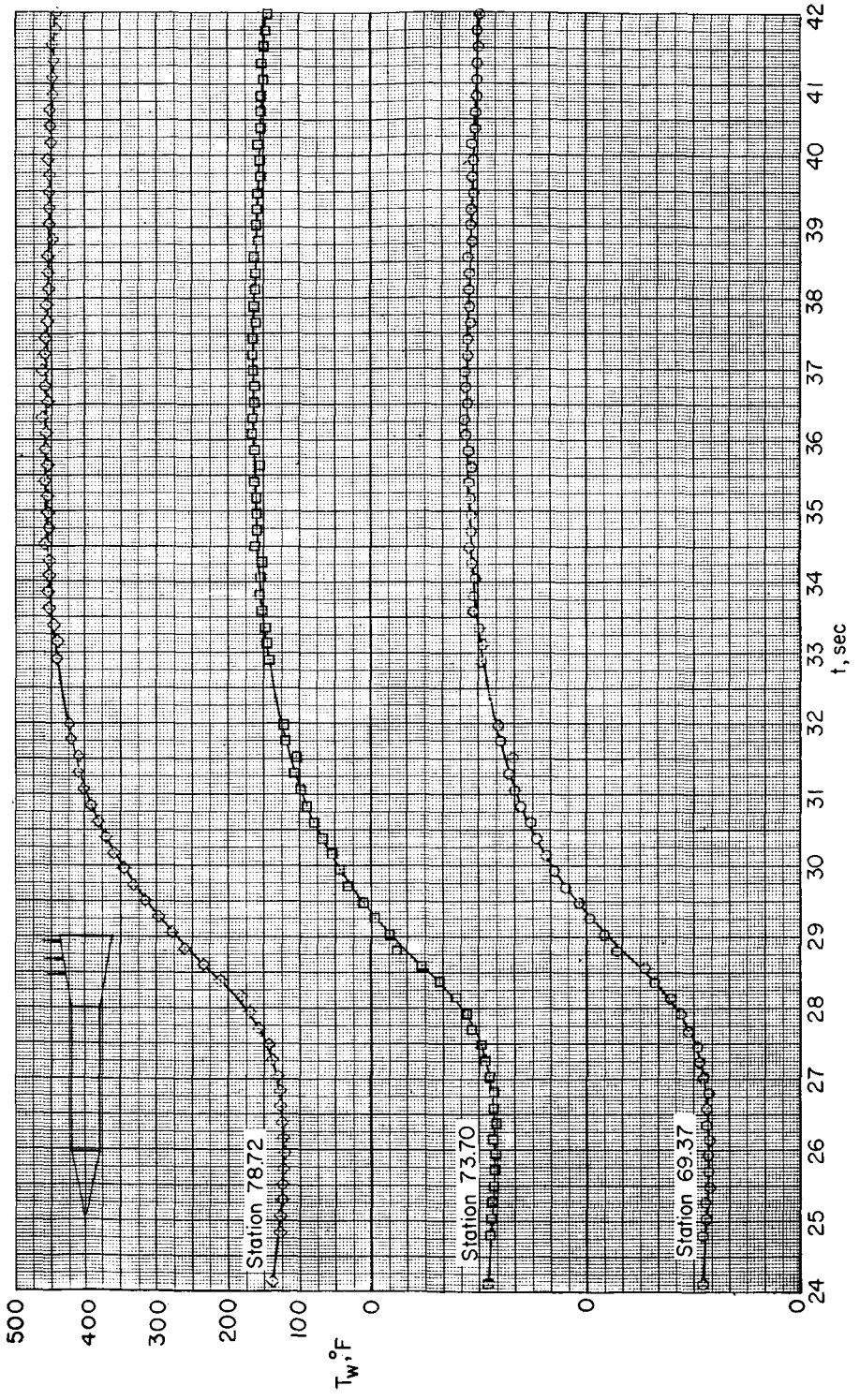

(e) Stations on rearward part of flare.

Figure 11.- Concluded.

[redacted]

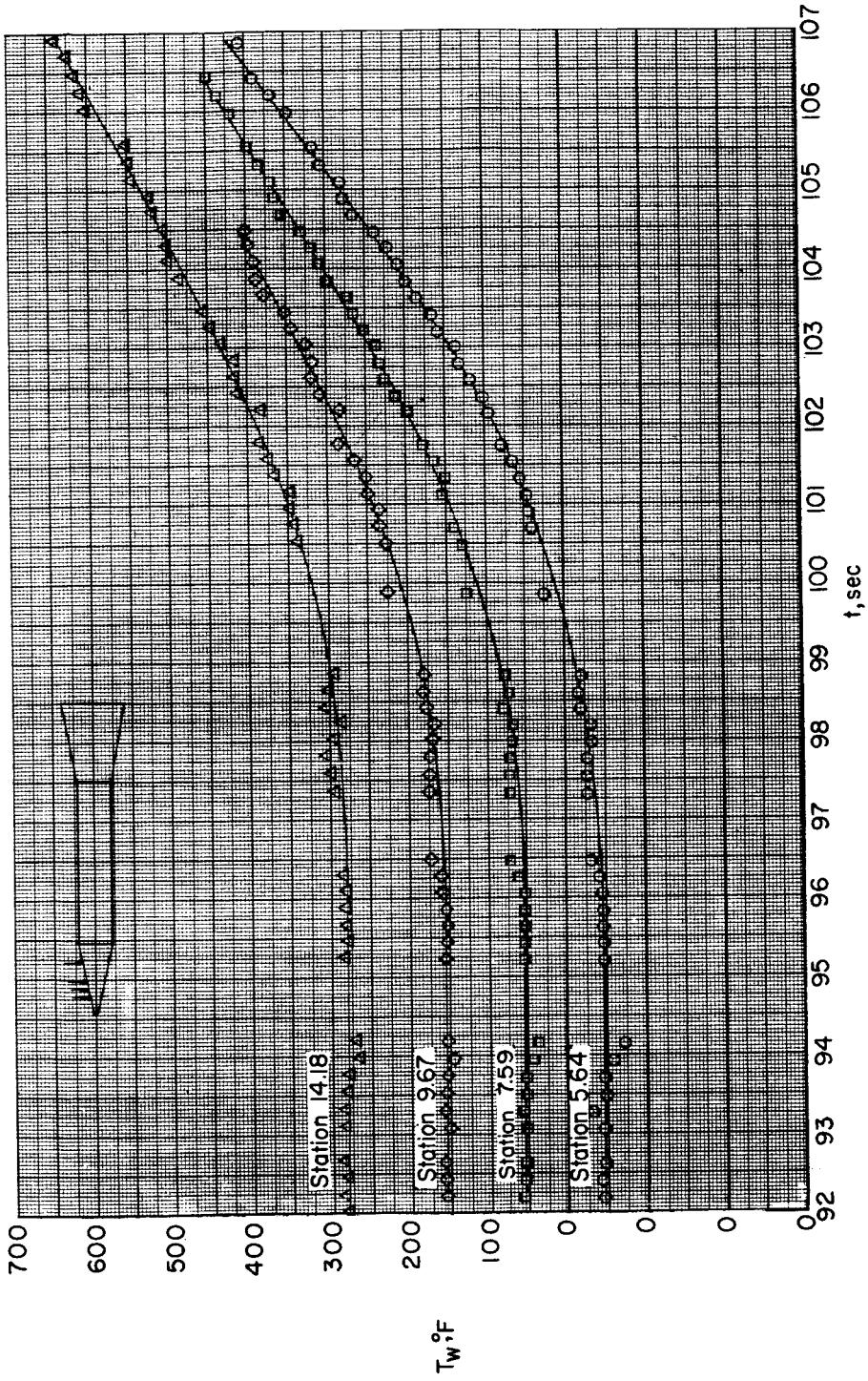

(a) Nose cone stations along upper thermocouple line.

Figure 12.- Time histories of skin temperatures over the period including the third- and fourth-stage burning.

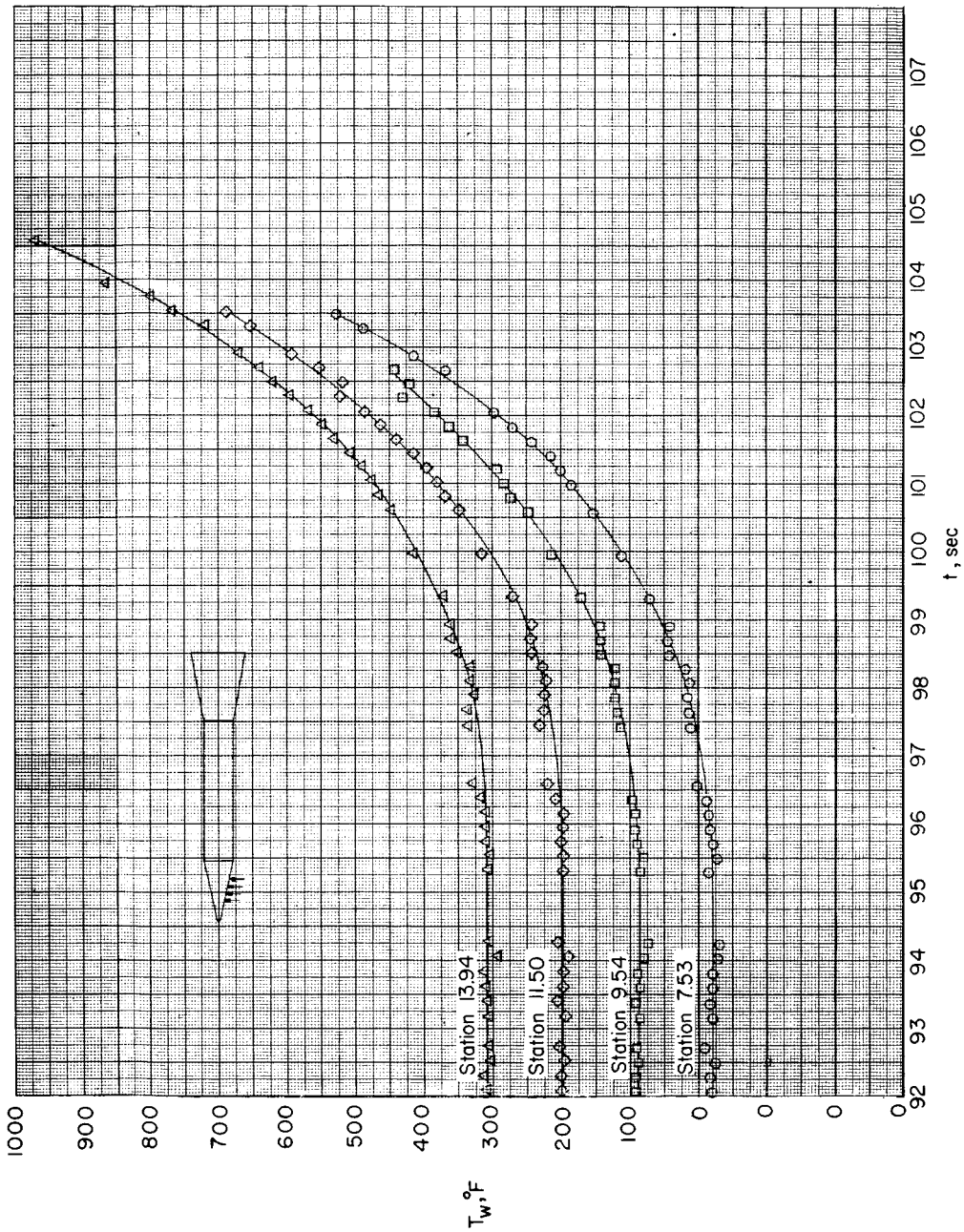

(b) Nose cone stations along lower thermocouple line.

Figure 12.- Continued.

[redacted]

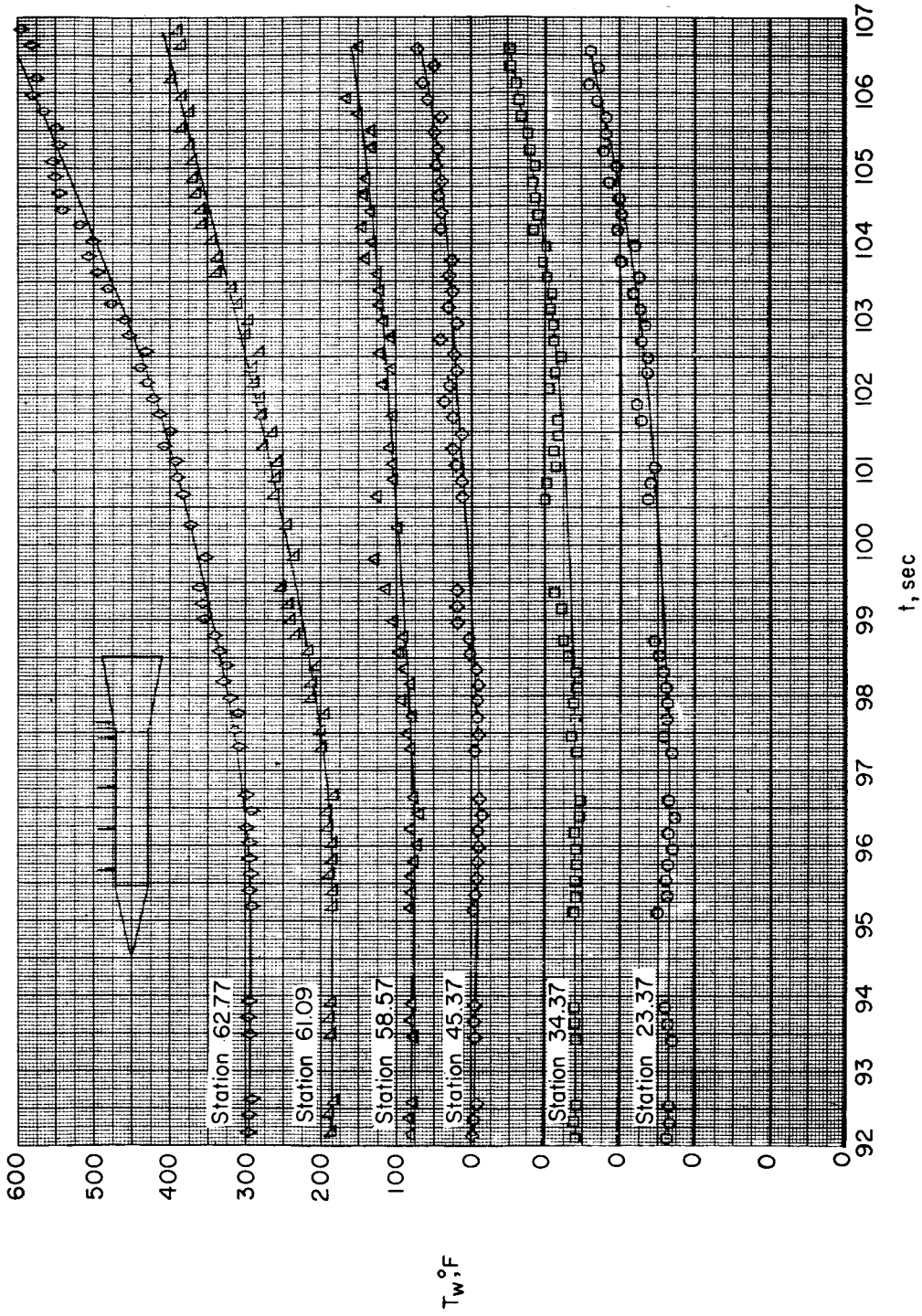

(c) Cylinder and forward flare stations.

Figure 12.- Continued.

[redacted]

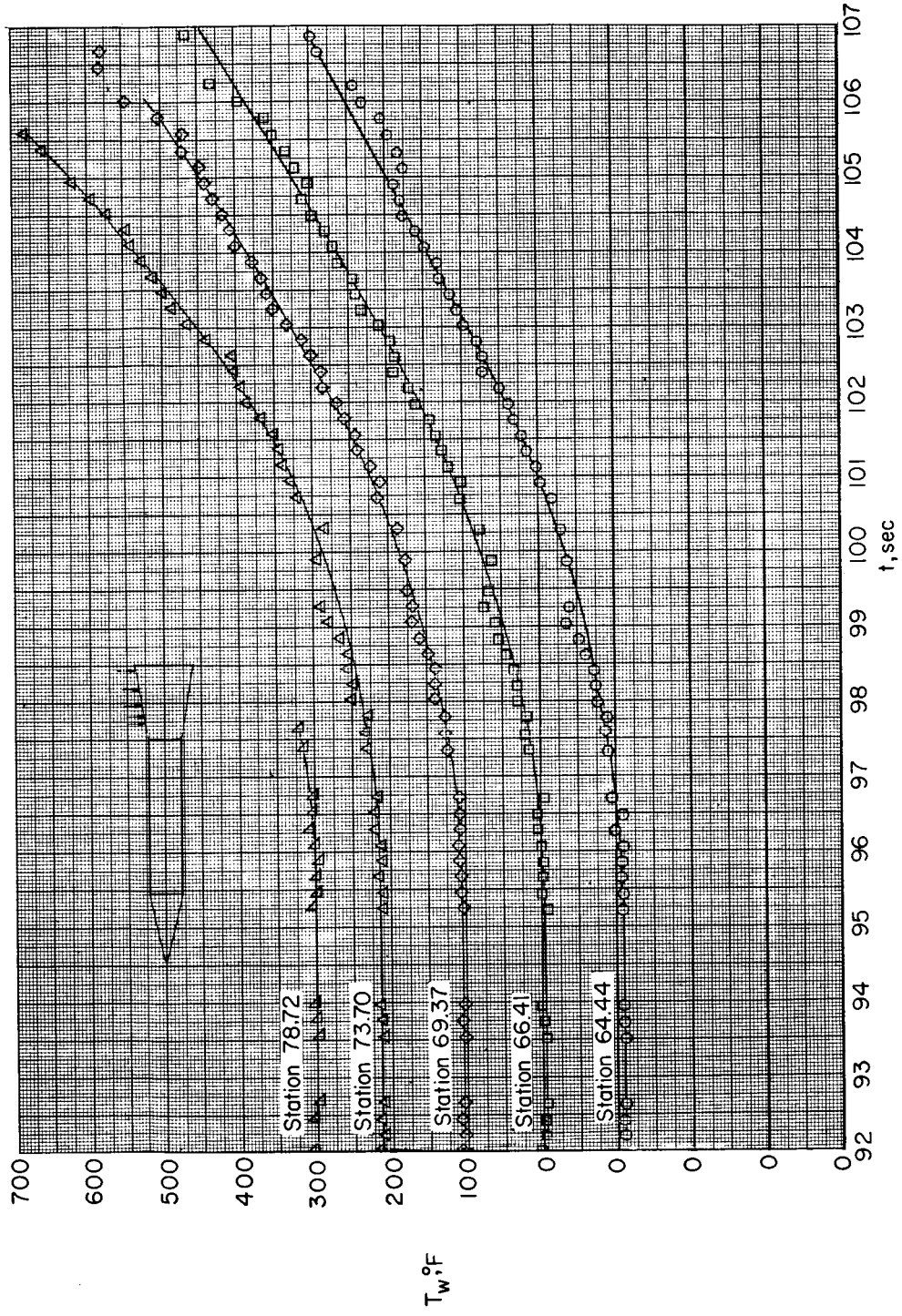

(d) Rearward flare stations.

Figure 12.- Concluded.

[redacted]

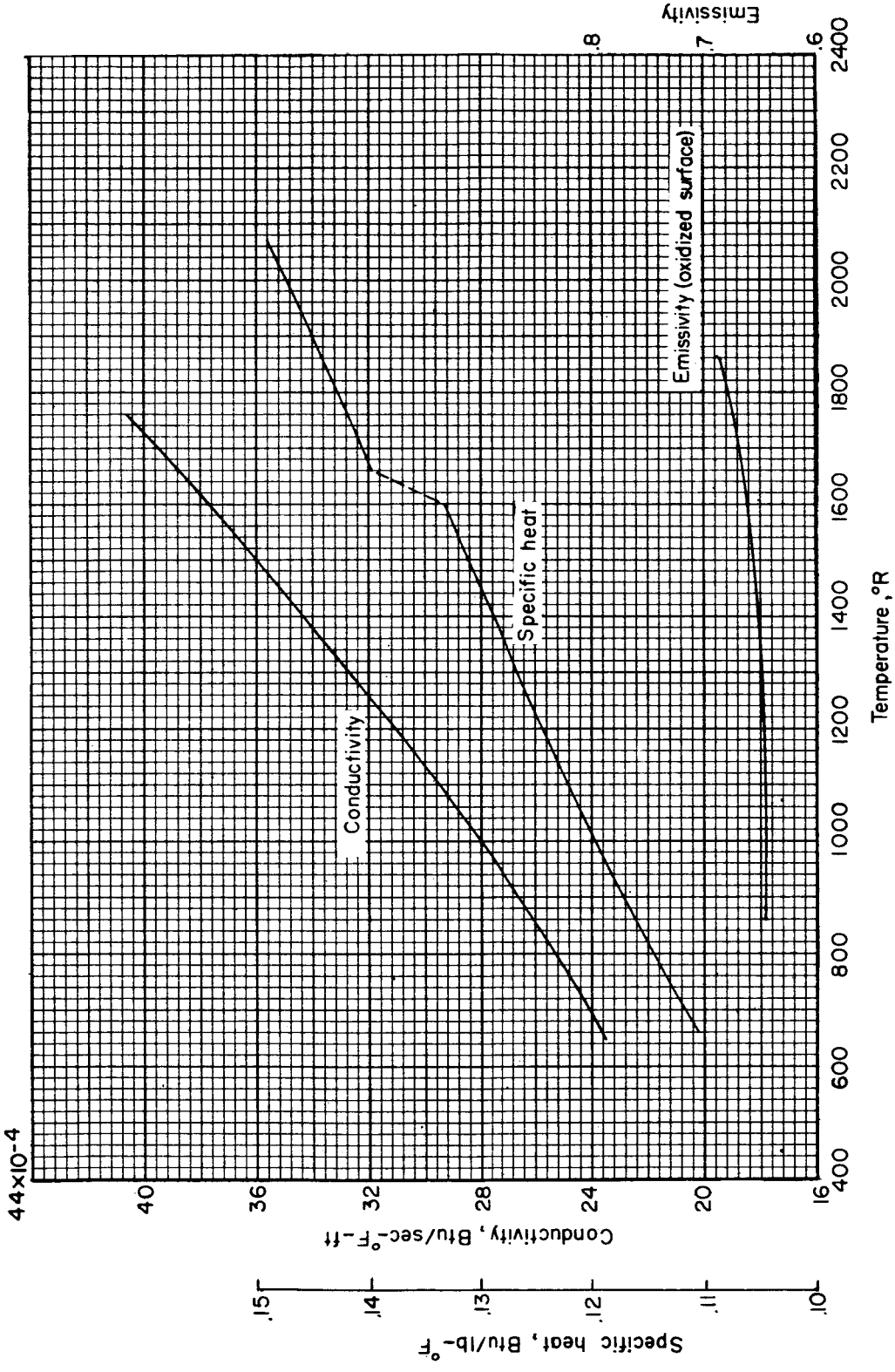

Figure 13.- Properties of annealed Inconel having 0.07-percent carbon content.

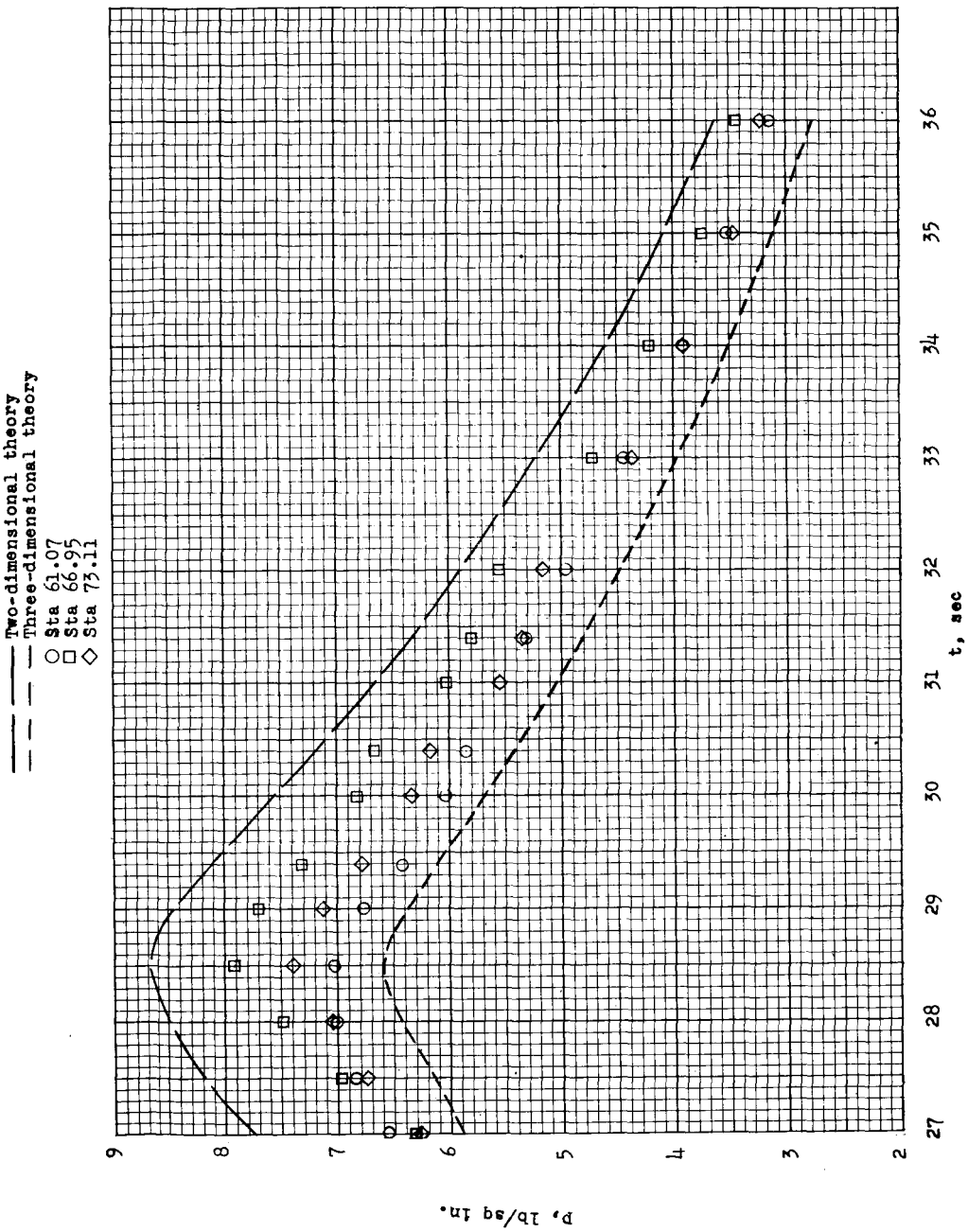

(a) At times from 27 to 36 seconds.

Figure 14.- Pressures on the flare.

[redacted]

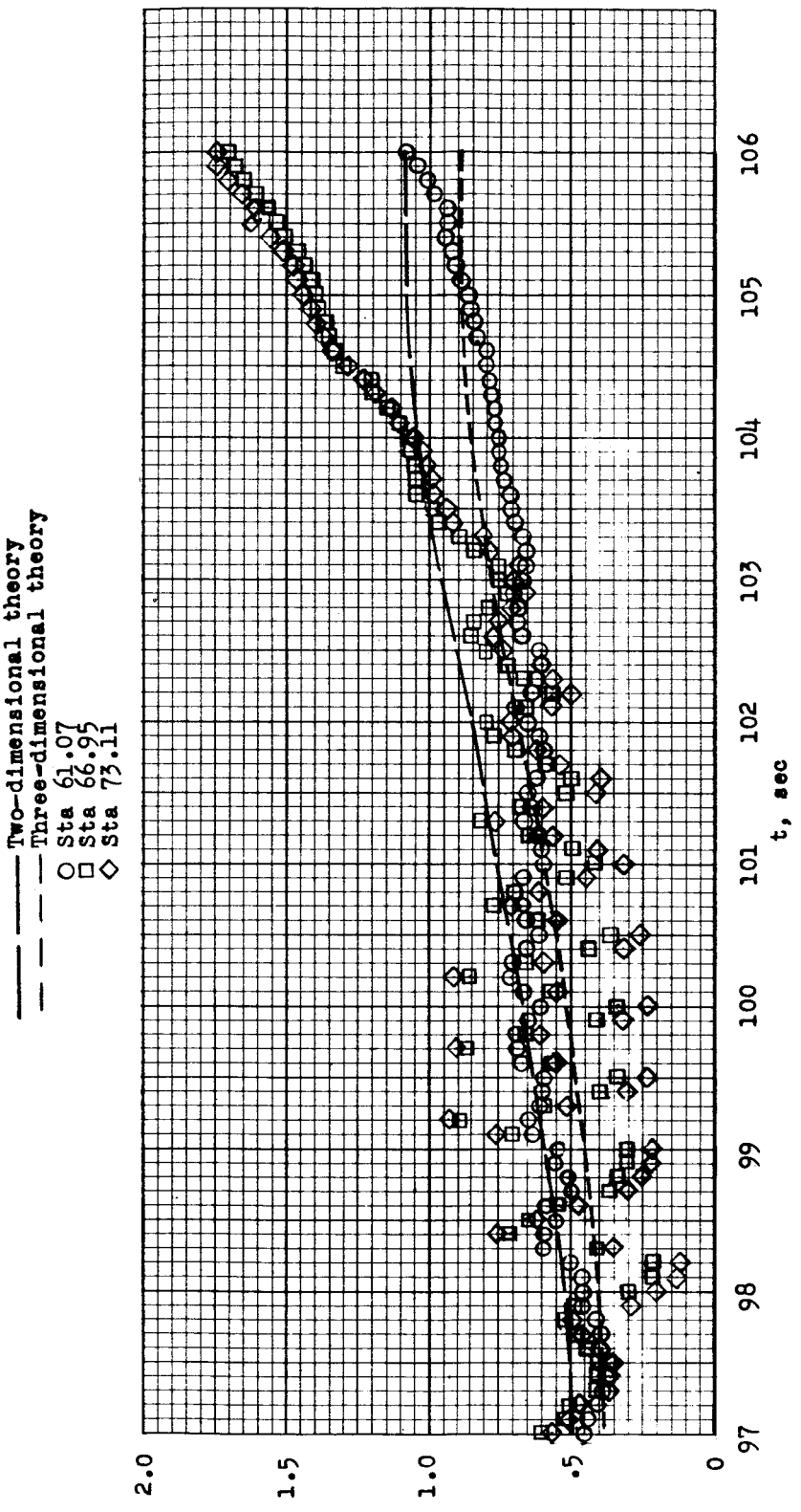

(b) At times from 97 to 106 seconds.

Figure 14.- Concluded.

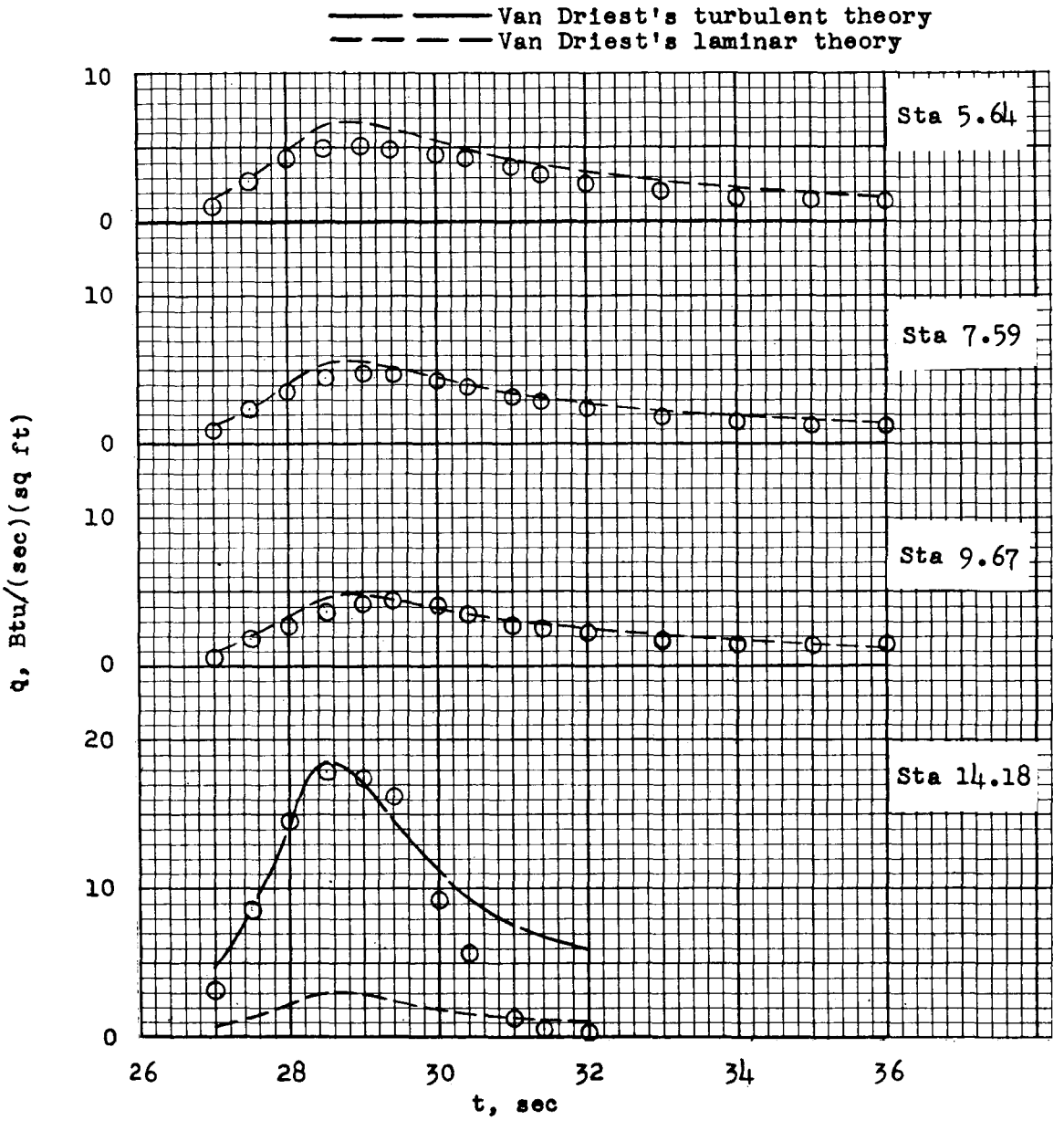

(a) Heating rates along the upper line on the nose cone.

Figure 15.- Experimental and theoretical heating rate comparisons at times 27 to 36 seconds.

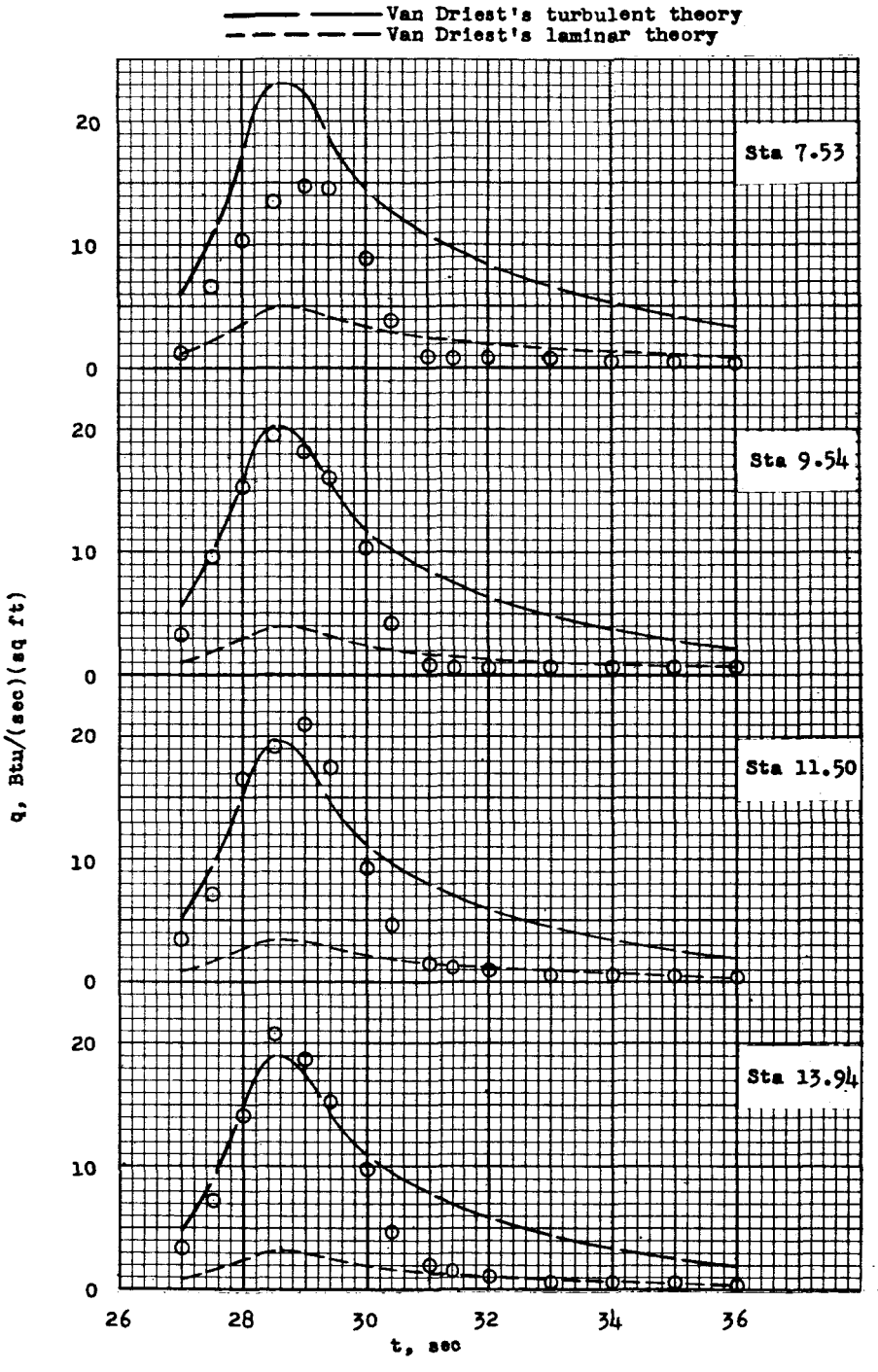

(b) Heating rates along the lower line on the nose cone.

Figure 15.- Continued.

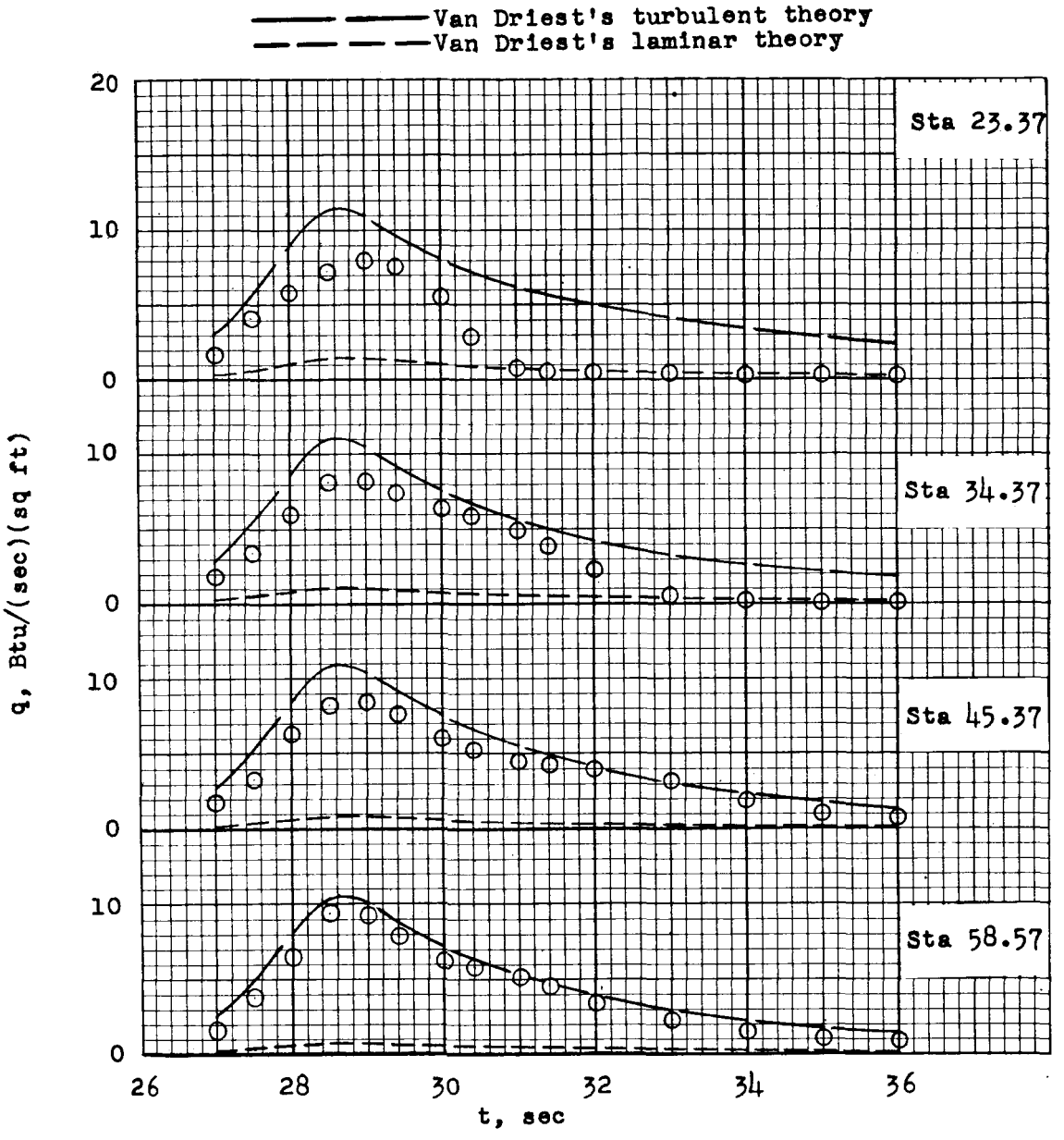

(c) Heating rates on the cylinder.

Figure 15.- Continued.

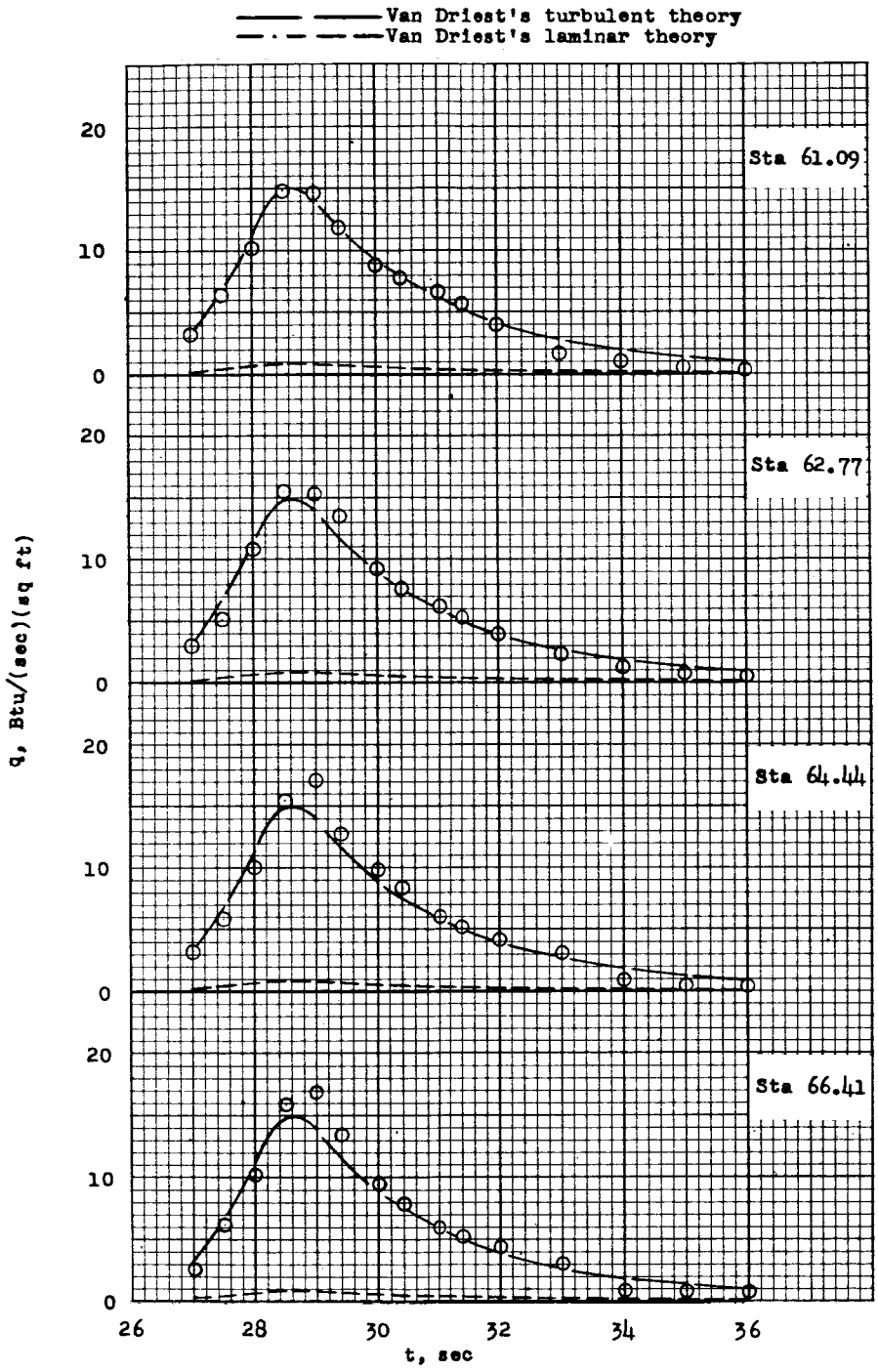

(d) Heating rates on the forward four stations of the flare.

Figure 15.- Continued.

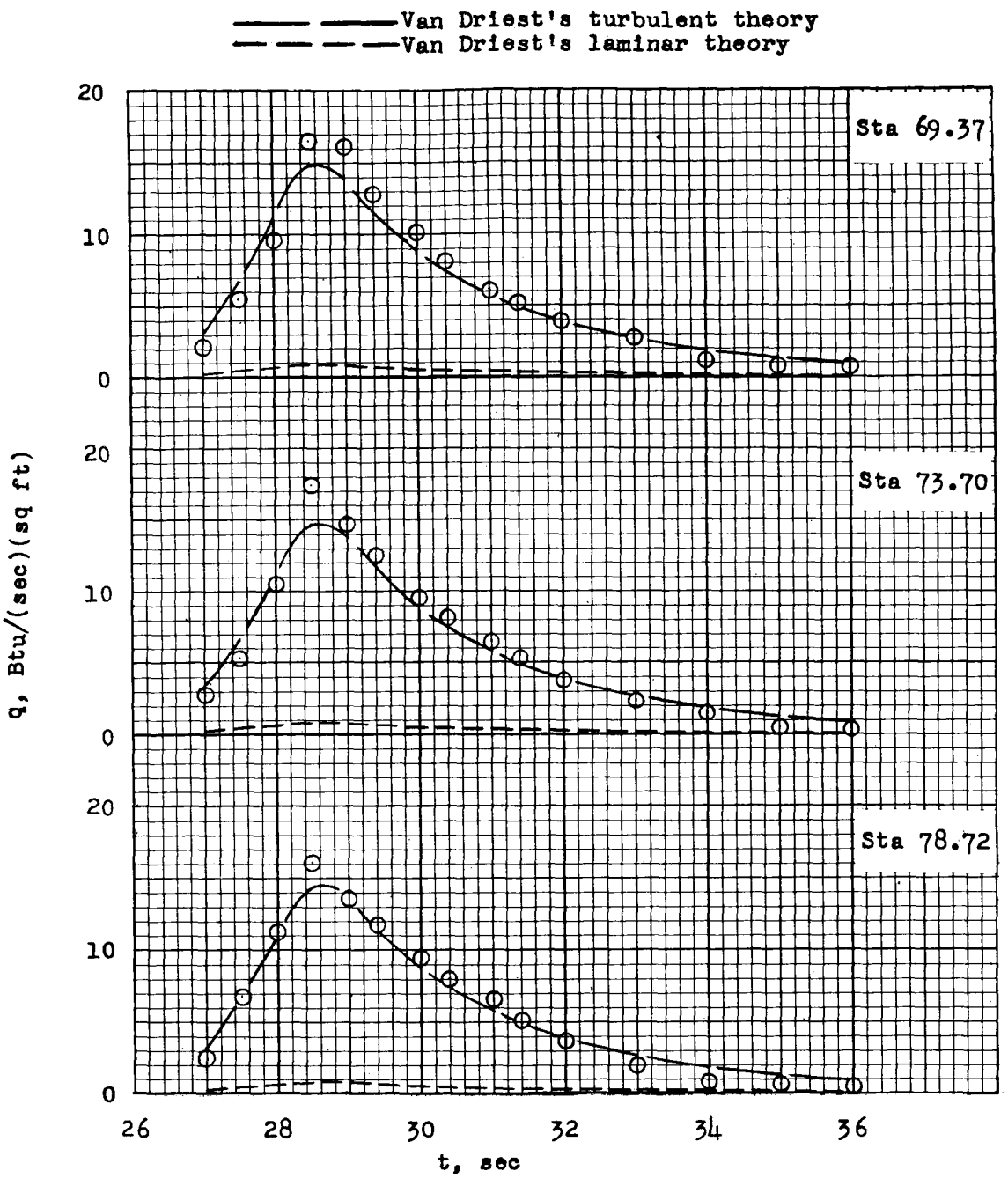

(e) Heating rates on the rearward three stations of the flare.

Figure 15.- Concluded.

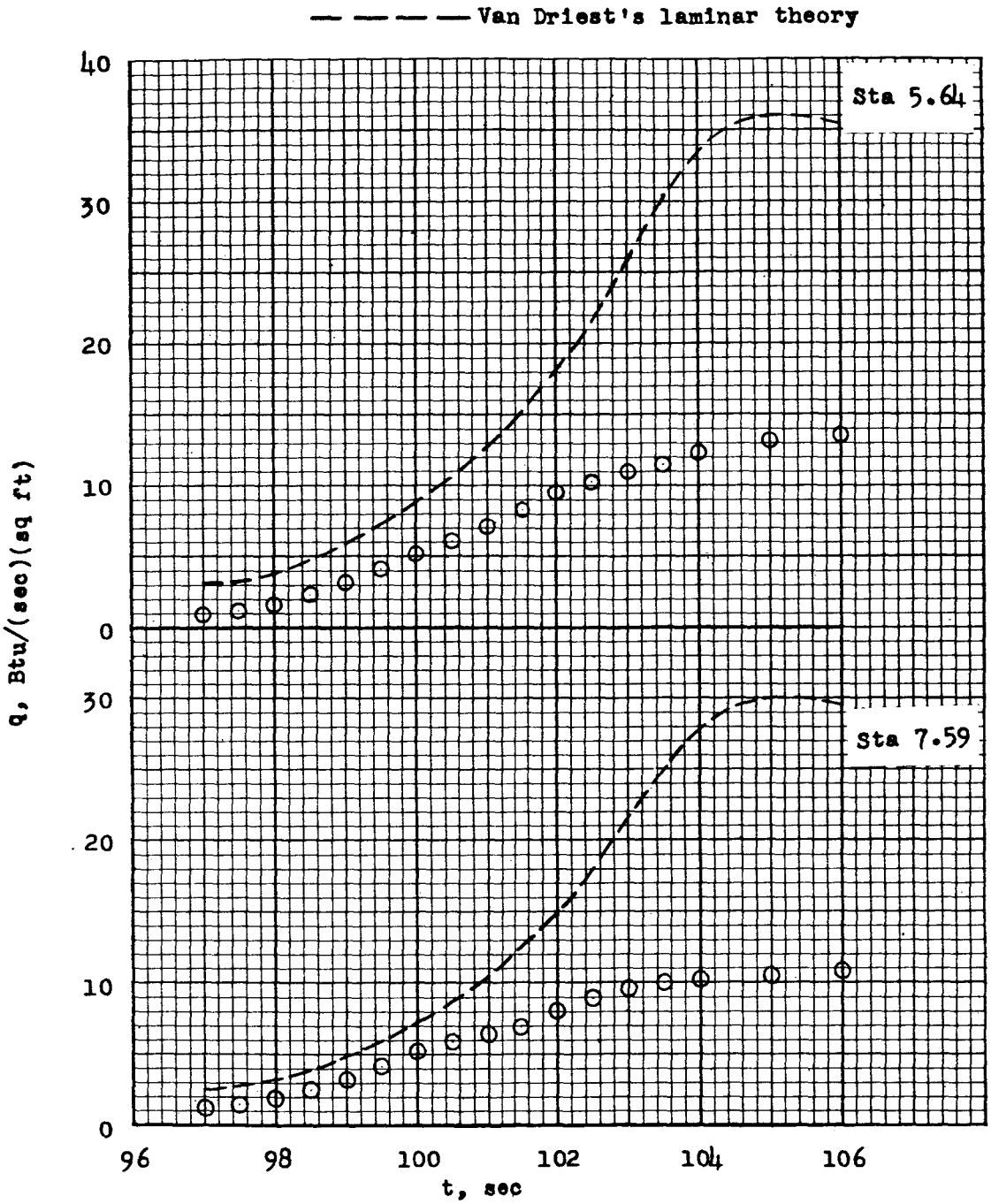

(a) Heating rates on the forward two stations on the upper line on the nose cone.

Figure 16.- Experimental and theoretical heating rates at times 97 to 106 seconds.

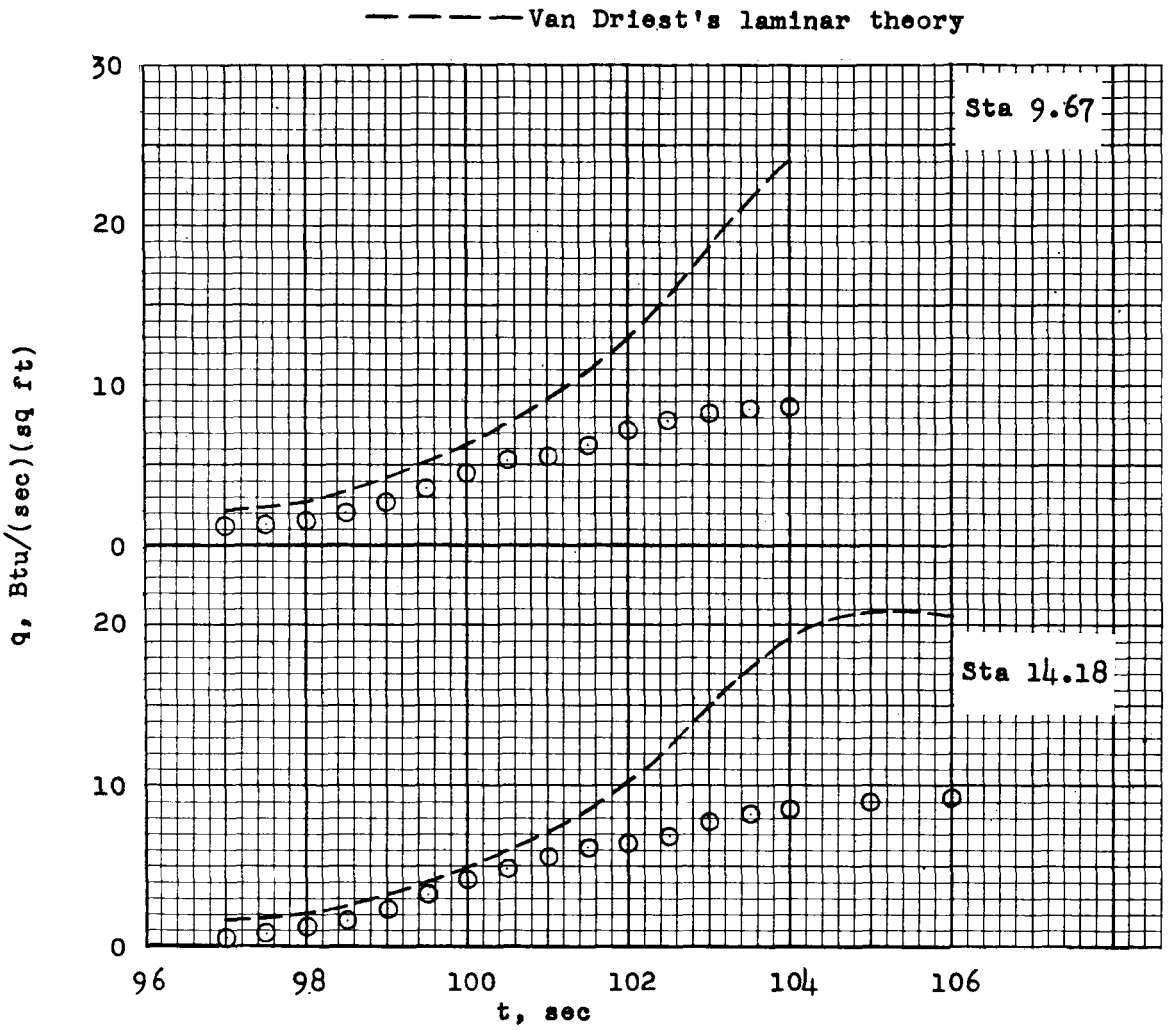

(b) Heating rates on the two rearward stations on the upper line on the nose cone.

Figure 16.- Continued.

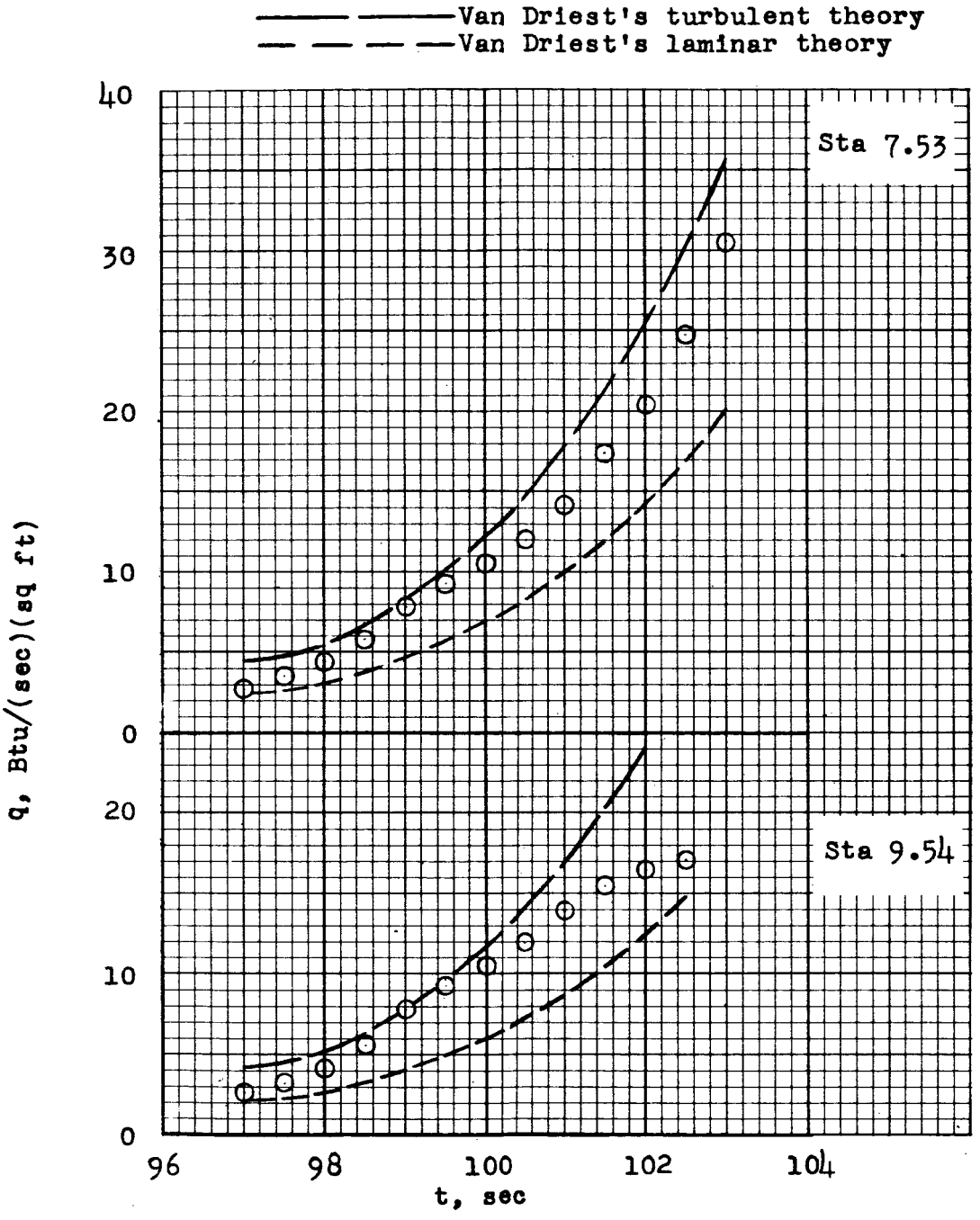

(c) Heating rates on the two forward stations on the lower line on the nose cone.

Figure 16.- Continued.

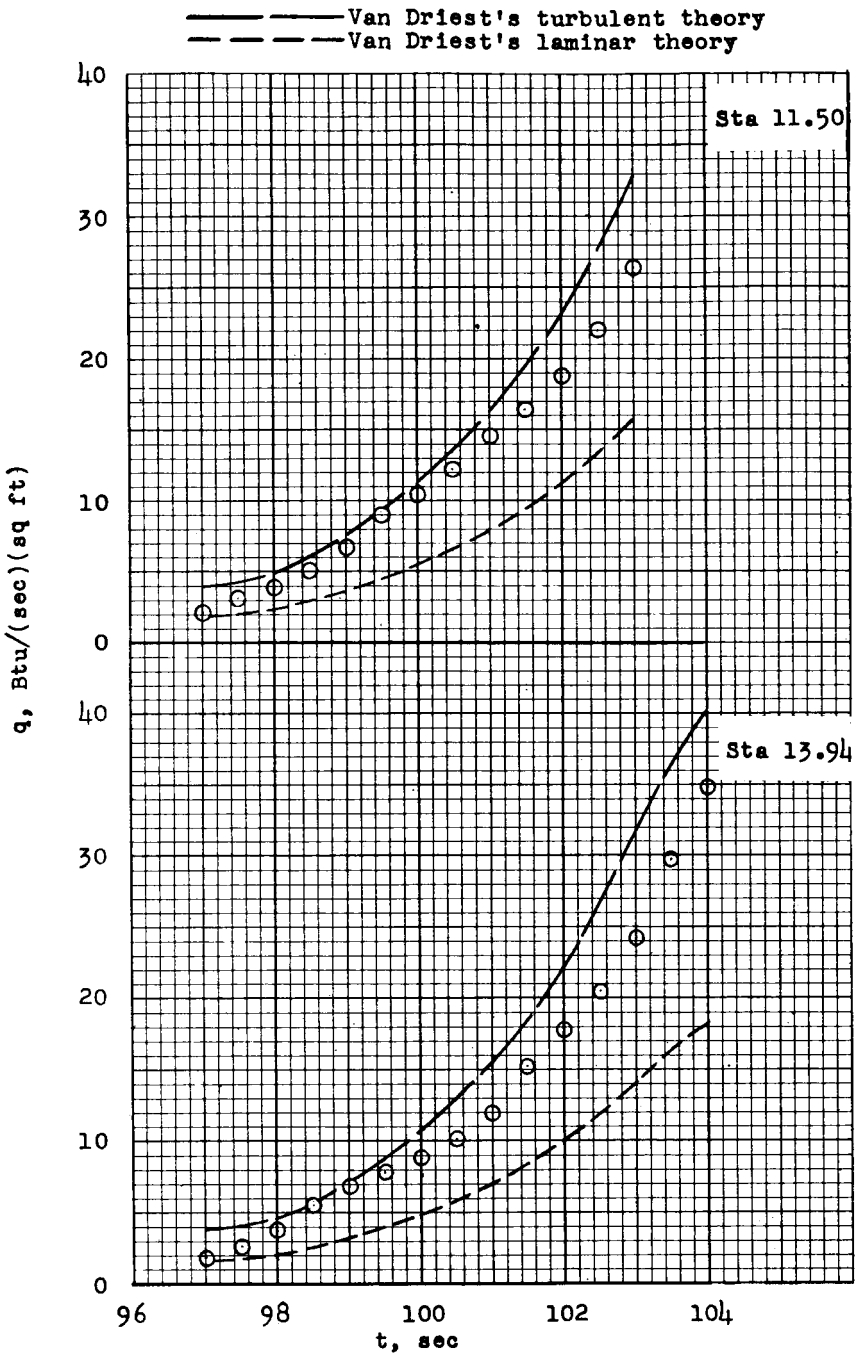

(d) Heating rates on the two rearward stations on the lower line on the nose cone.

Figure 16.- Continued.

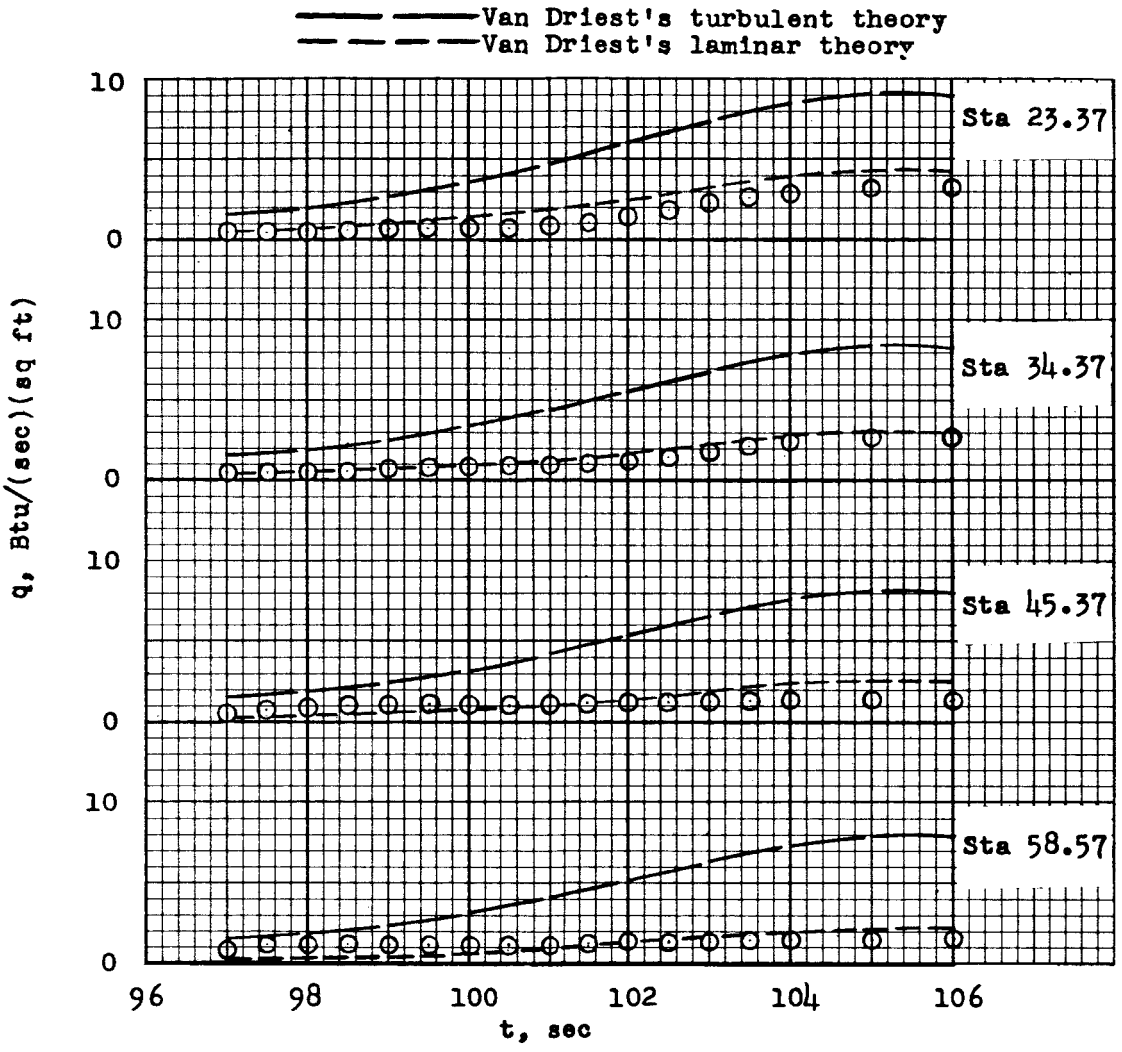

(e) Heating rates on the cylinder.

Figure 16.- Continued.

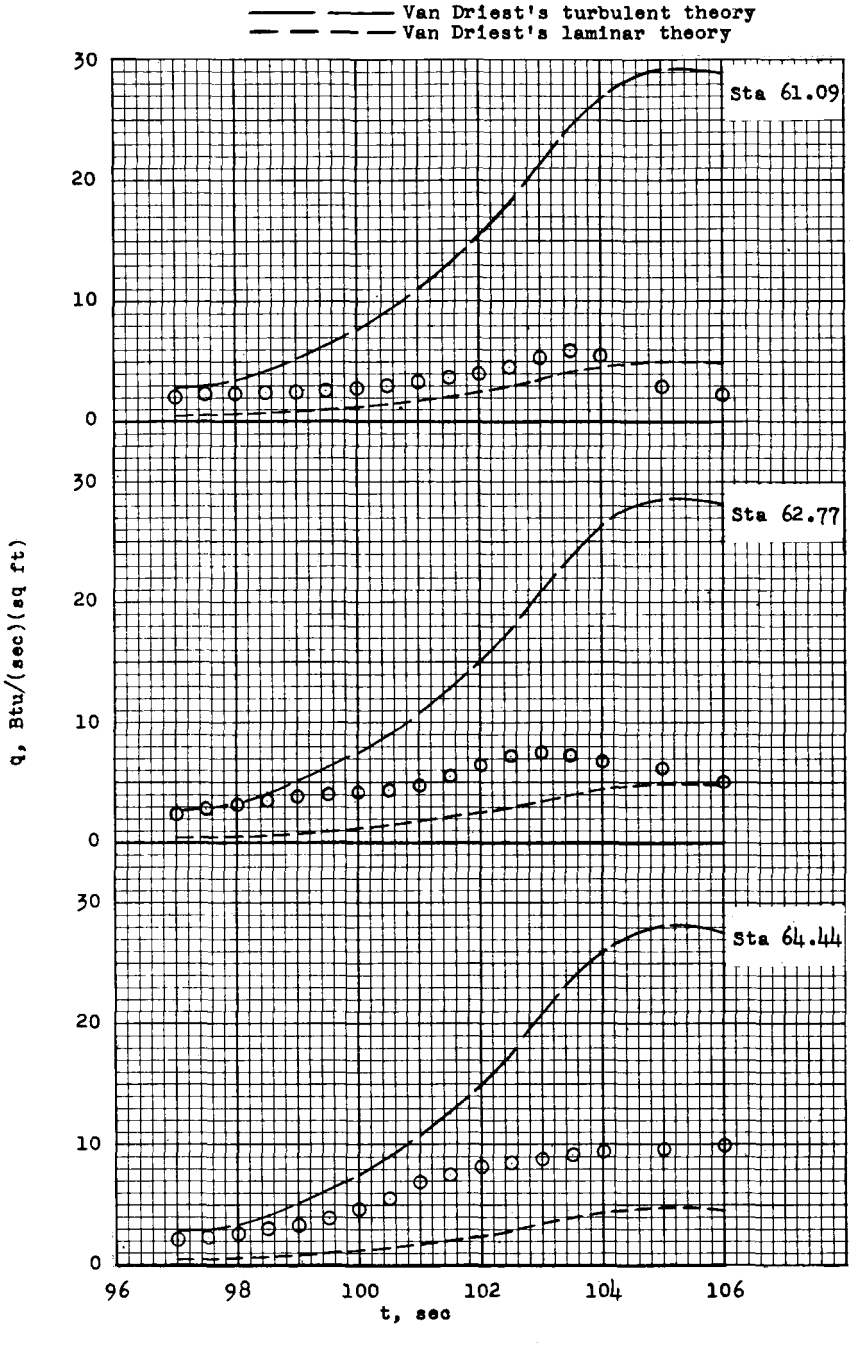

(f) Heating rates on the three forward stations of the flare.

Figure 16.- Continued.

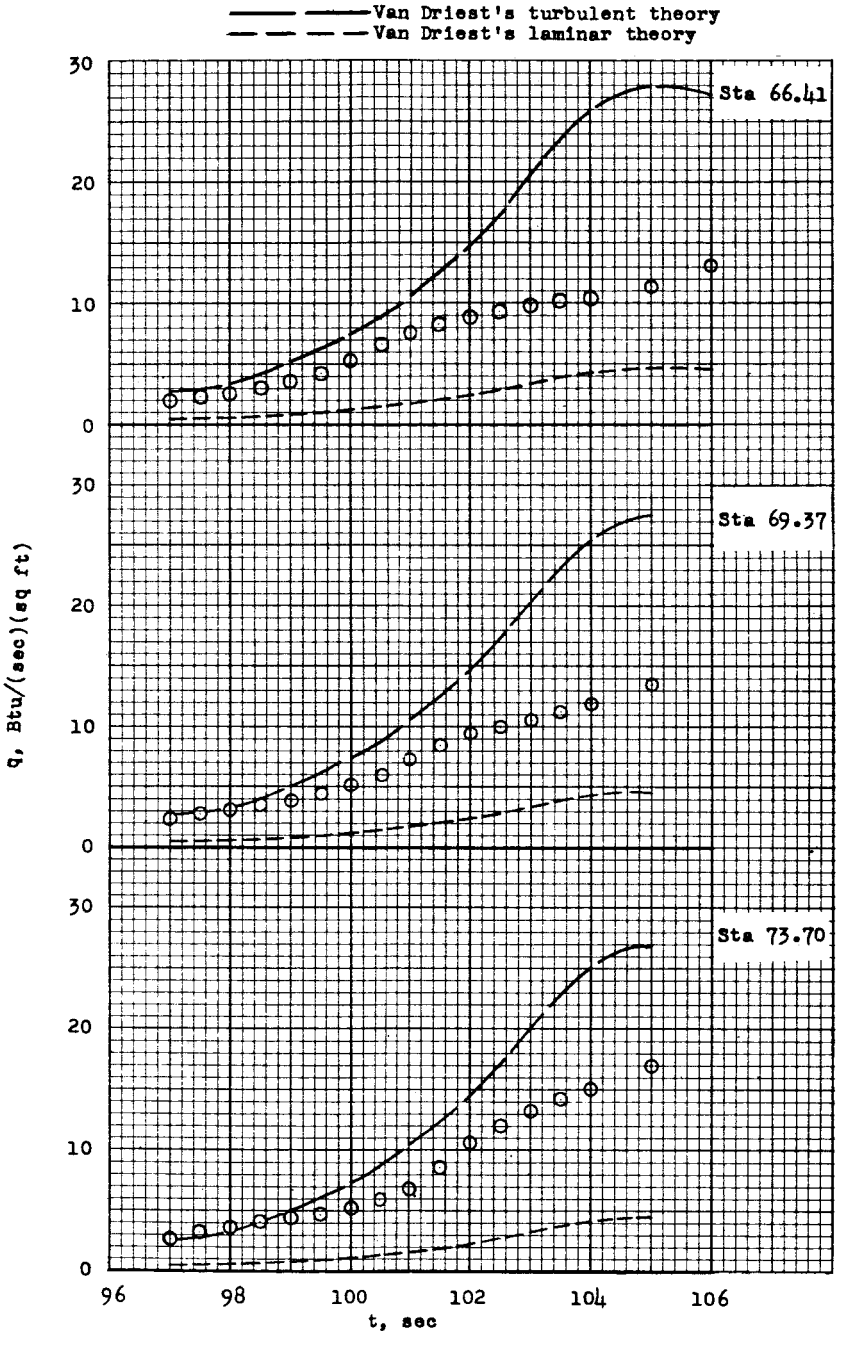

(g) Heating rates on the three rearward flare stations which recorded at this time.

Figure 16.- Concluded.

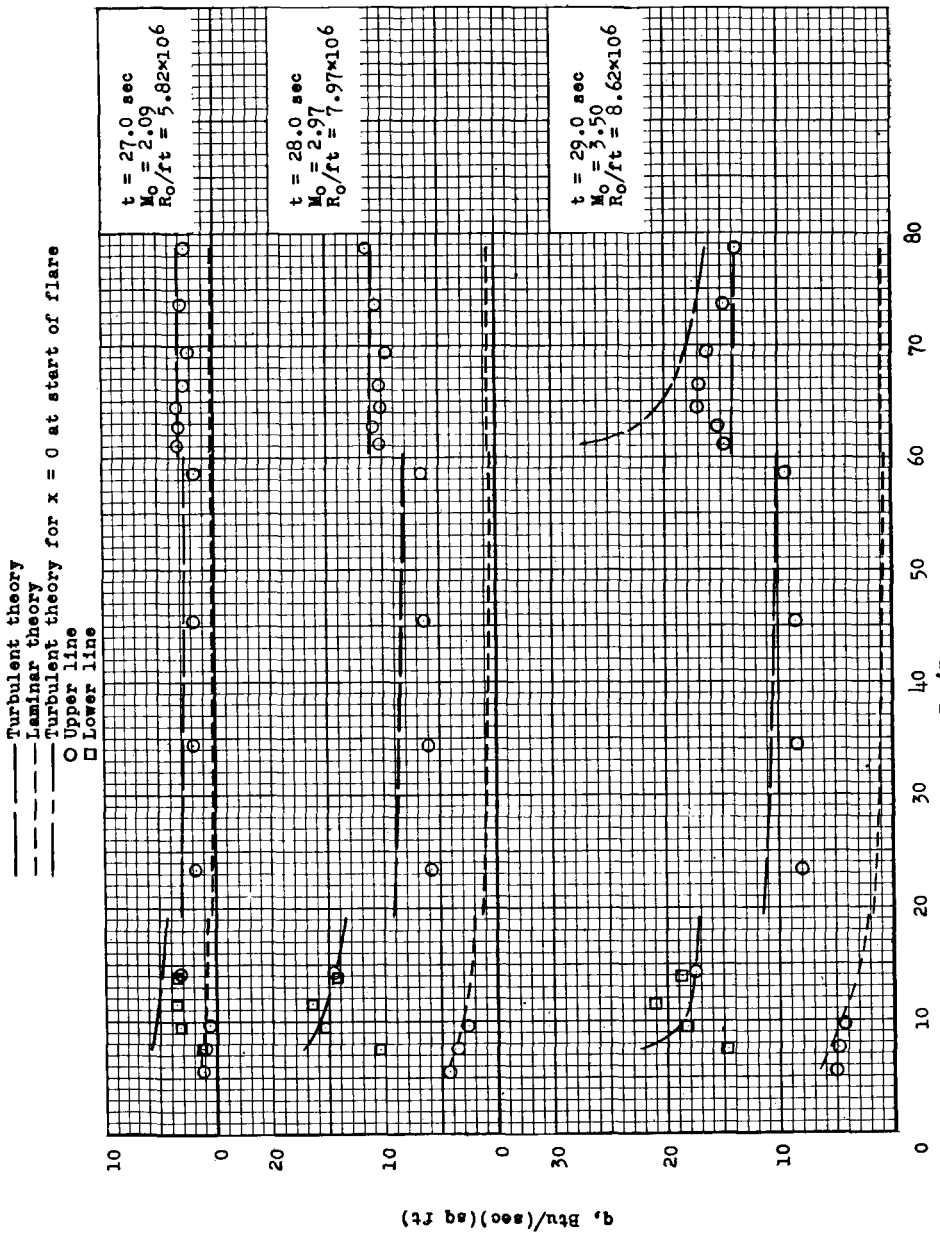

(a) For times 27.0, 28.0, and 29.0 seconds.

Figure 17.- Distribution of experimental and theoretical heating rates along the nose, cylinder, and flare.

[redacted]

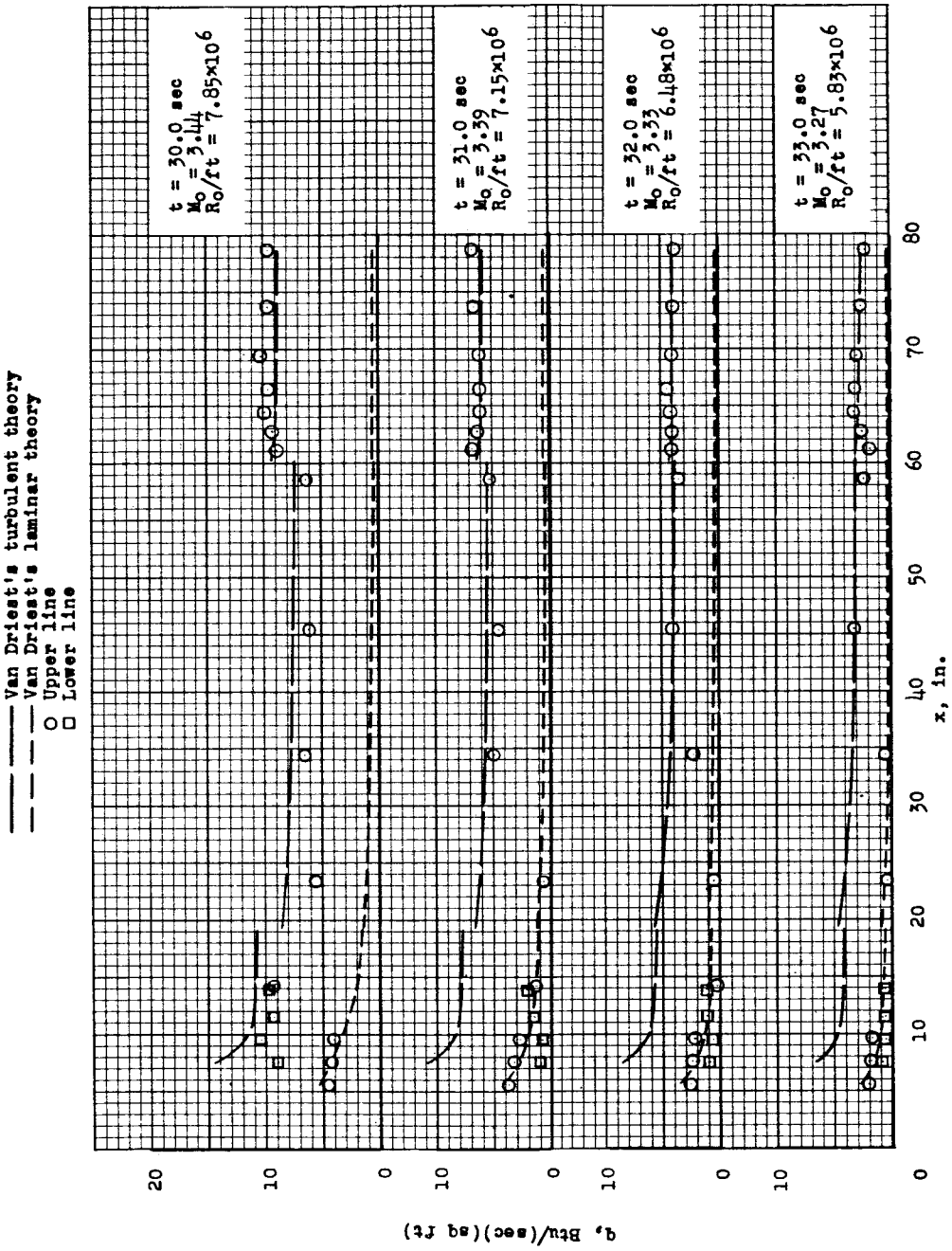

(b) For times 30.0, 31.0, 32.0, and 33.0 seconds.

Figure 17.- Continued.

[redacted]

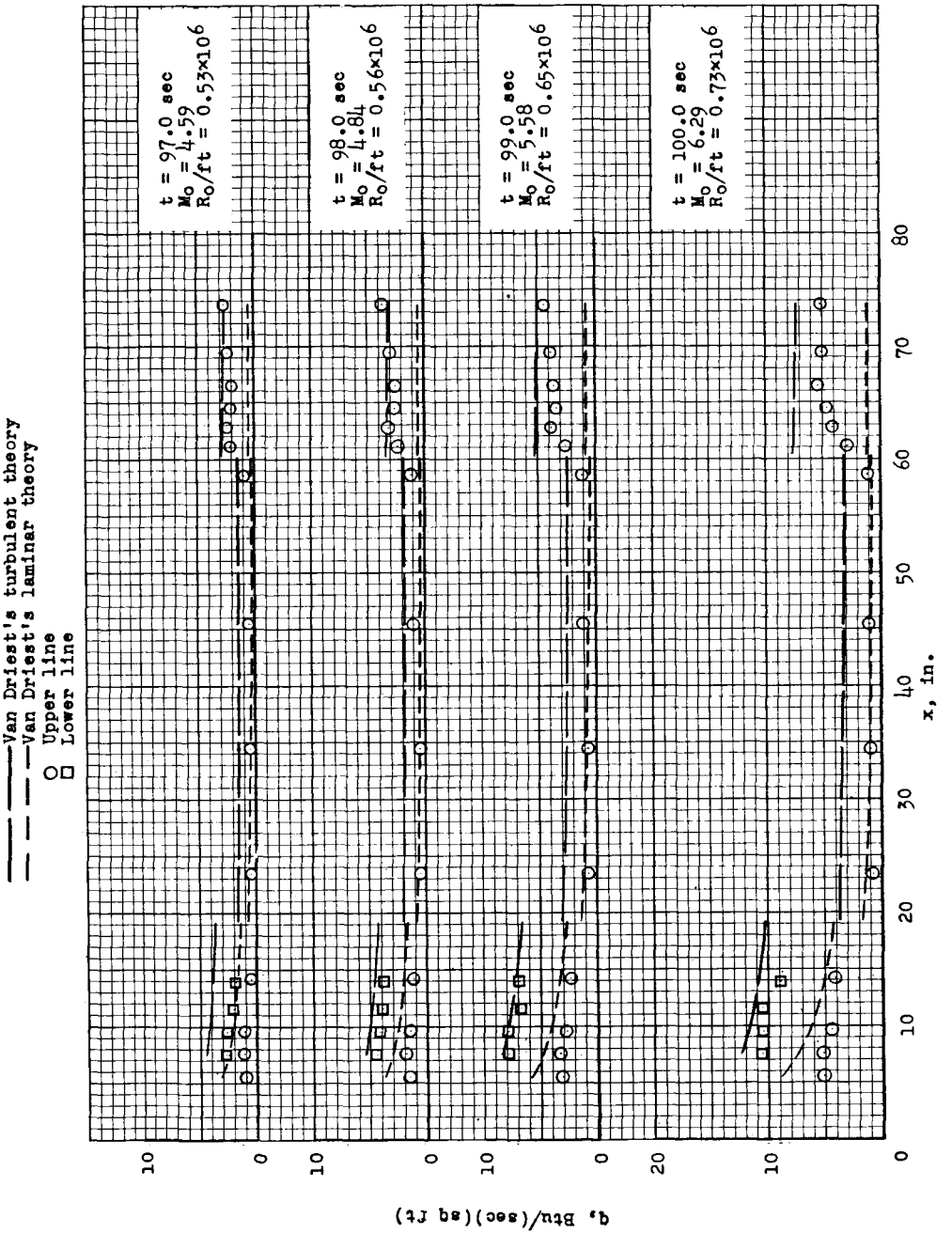

(c) For times 97.0, 98.0, 99.0, and 100.0 seconds.

Figure 17.- Continued.

[redacted]

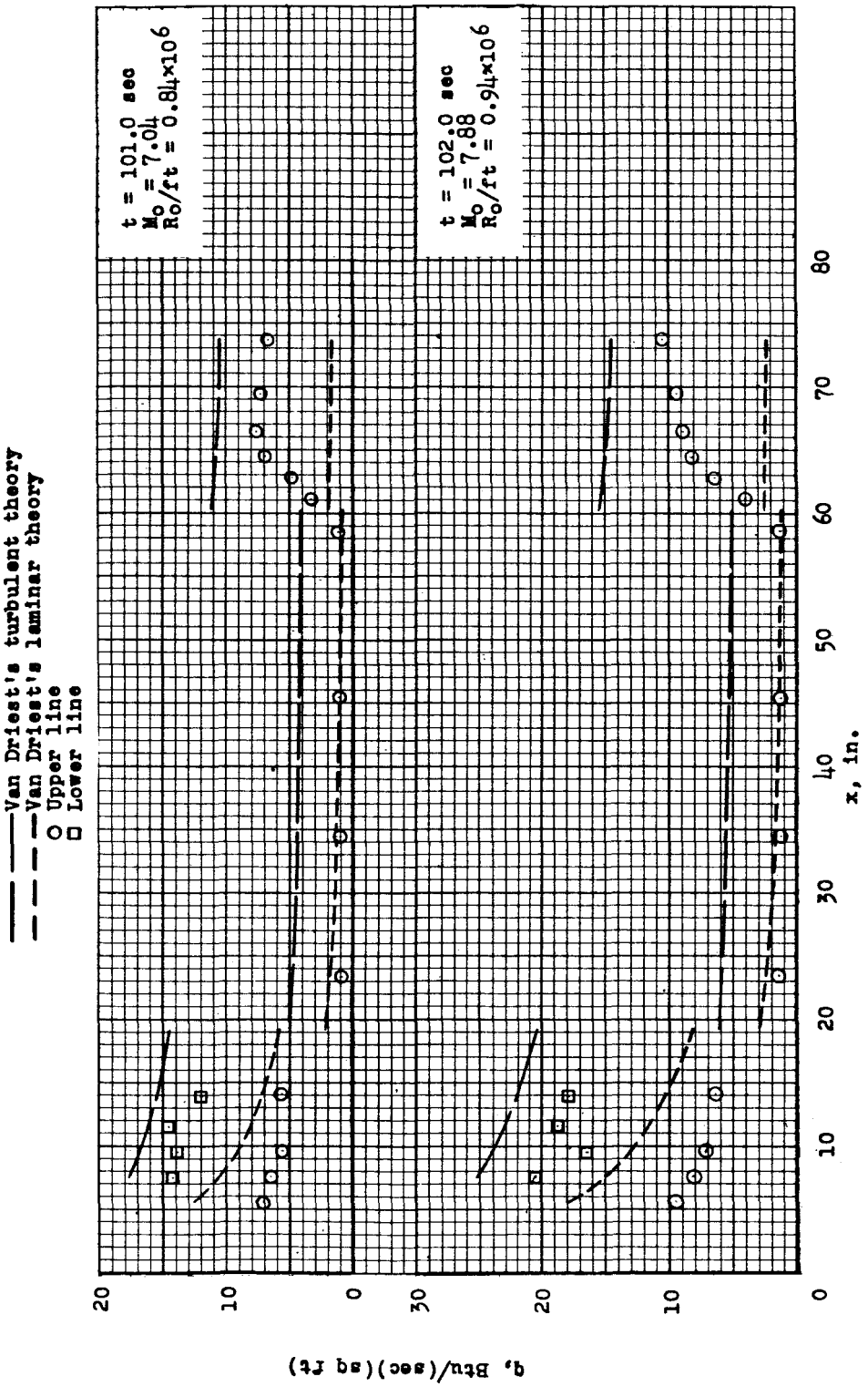

(d) For times 101.0 and 102.0 seconds.

Figure 17.- Continued.

[redacted]

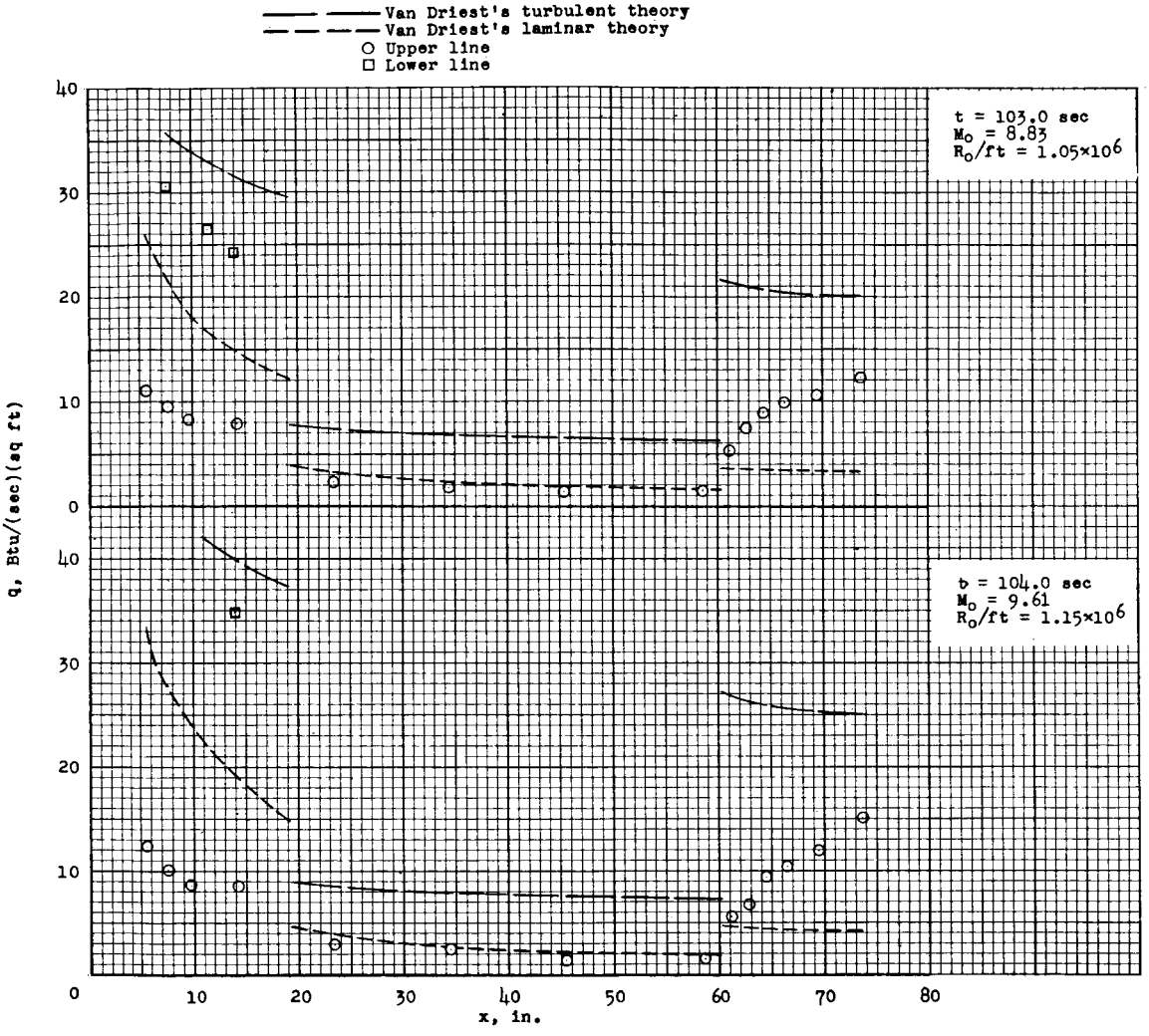

(e) For times 103.0 and 104.0 seconds.

Figure 17.- Continued.

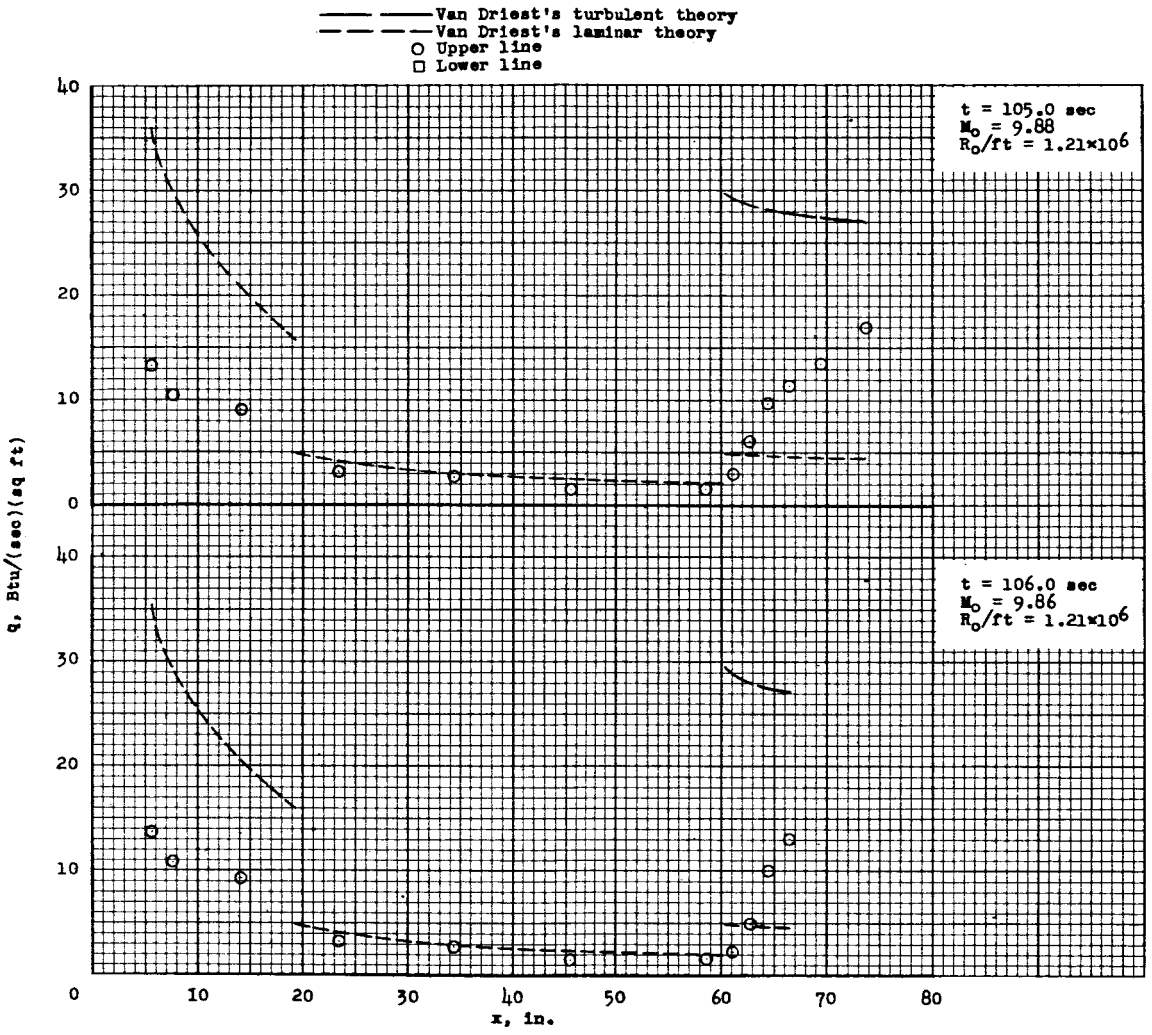

(f) For times 105.0 and 106.0 seconds.

Figure 17.- Concluded.

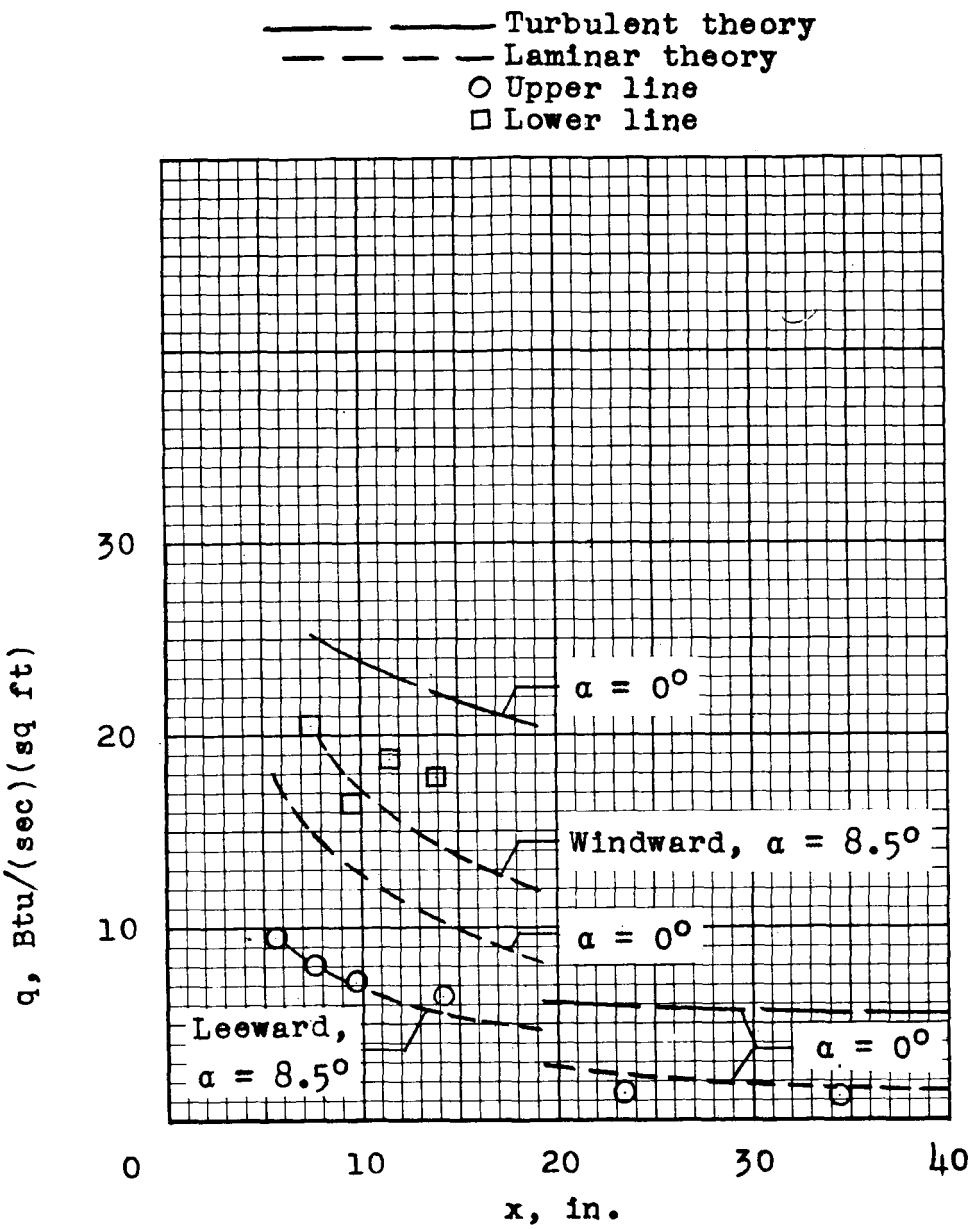

(a) At time 102 seconds for assumed angle of attack of 8.5°.

Figure 18.- Comparison of heating rates measured on the nose cone with theory for angle-of-attack conditions.

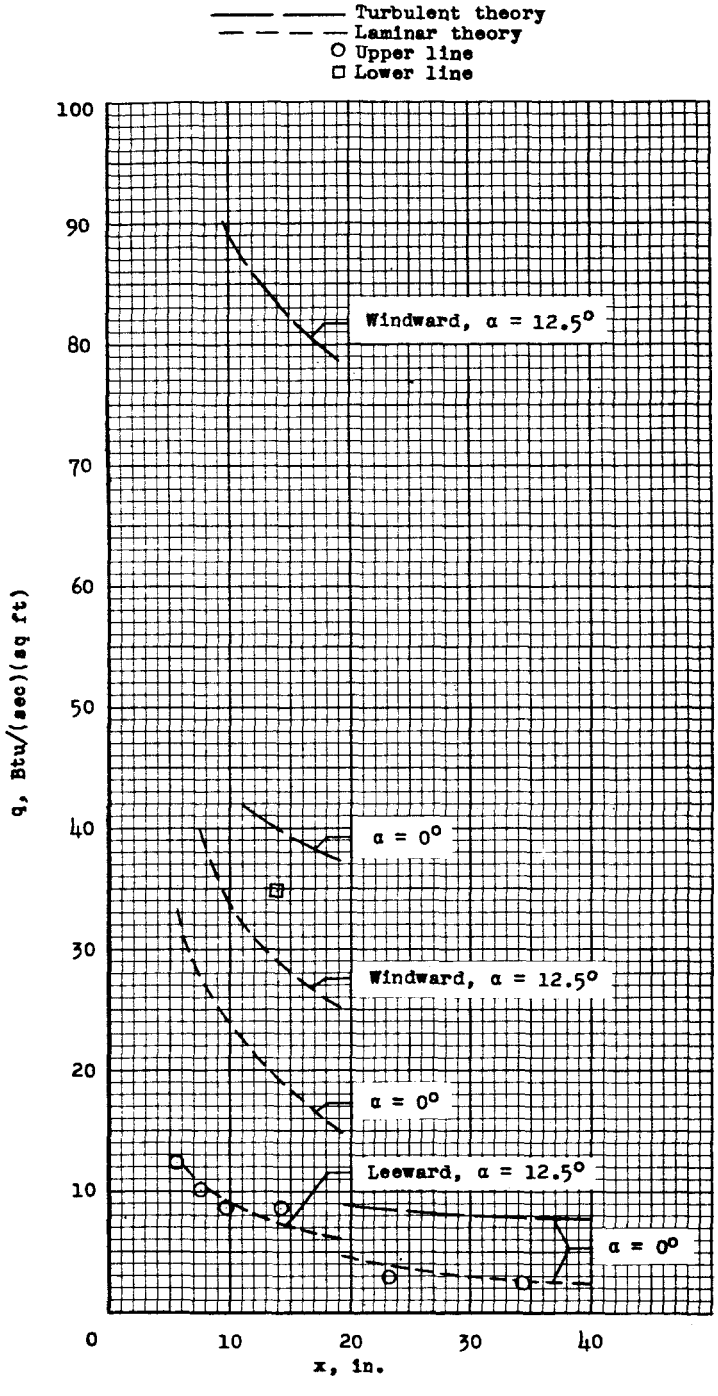

(b) At time 104 seconds for assumed angle of attack of 12.5°.

Figure 18.- Concluded.

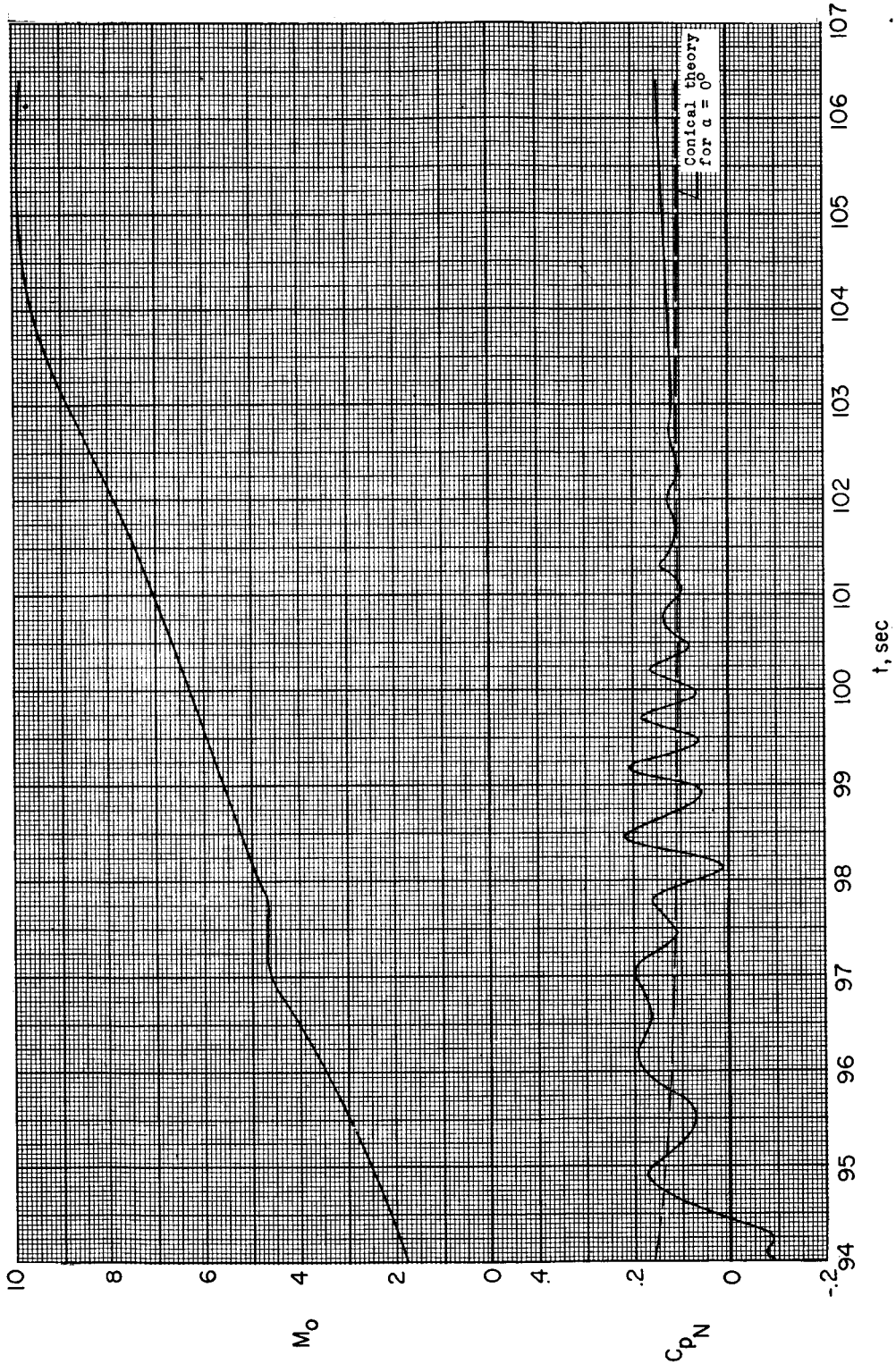

Figure 19.- Variation of nose pressure coefficient and Mach number with time during the high-speed portion of flight.

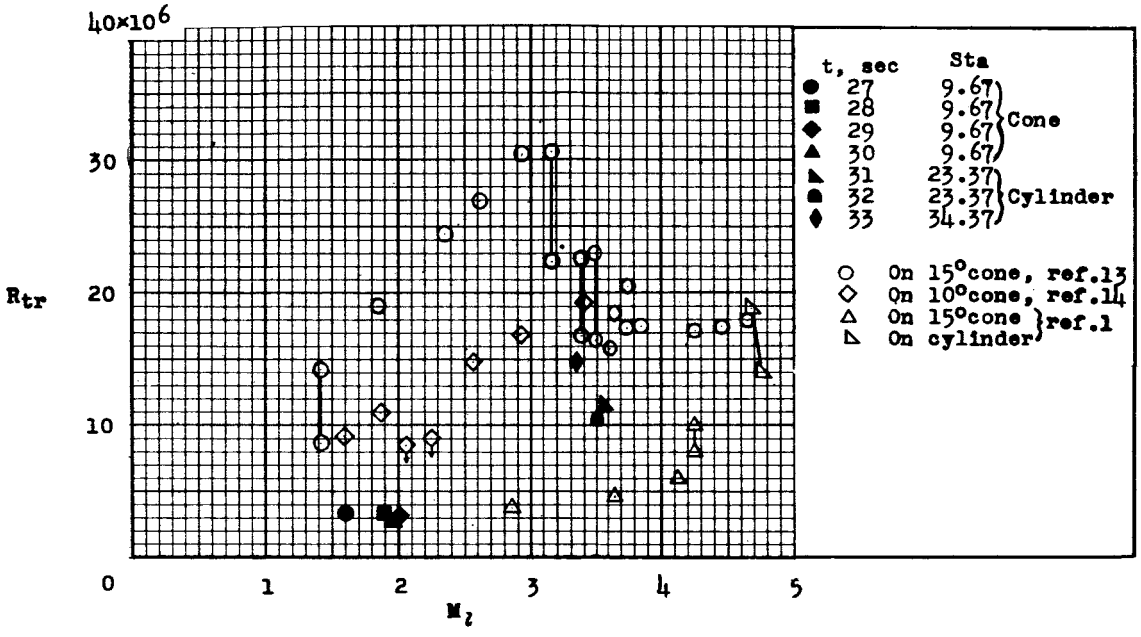

(a) R_{tr} as a function of M_l.

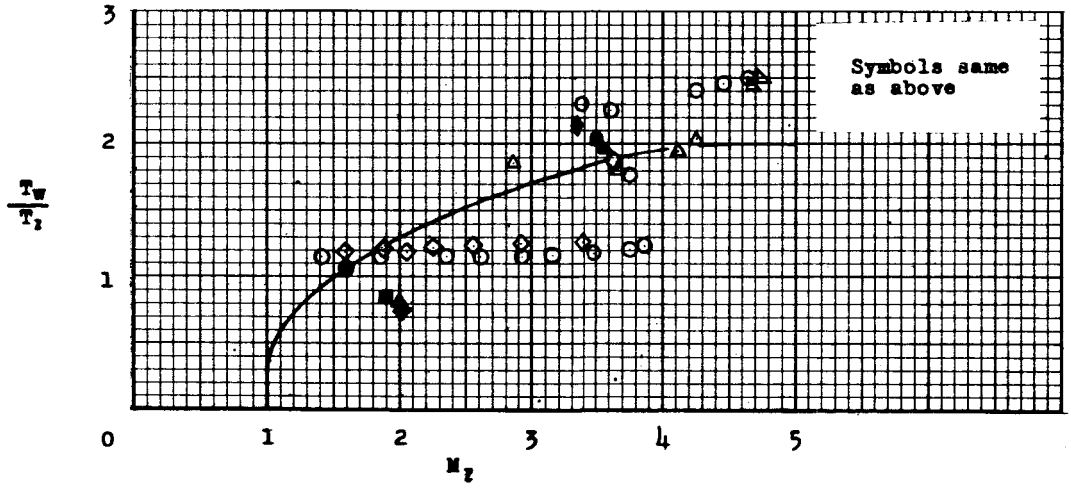

(b) Condition at transition.

Figure 20.- Boundary-layer transition measurements.

[redacted]

DECLASSIFIED

CONFIDENTIAL

CONFIDENTIAL